DOI:
10.1071/WF16178

Document Version
Peer reviewed version

Link to publication record in King's Research Portal

Publisher: CSIRO; Journal: WF:International Journal of Wildland Fire
Article Type: research-article; Volume: ; Issue: ; Article ID: WF16178
DOI: 10.1071/WF16178; TOC Head:

Direct estimation of Byram's fire intensity from infrared remote sensing imagery

Joshua M. Johnston[A,B,E], *Martin J. Wooster*[B,C], *Ronan Paugam*[B,D], *Xianli Wang*[A], *Timothy J. Lynham*[A] *and Lynn M. Johnston*[A]

[A]Canadian Forest Service, Great Lakes Forestry Centre, 1219 Queen Street E, Sault Ste Marie, ON, P6A 2E5, Canada.

[B]King's College London, Department of Geography, Strand, London WC2R 2LS, UK.

[C]Natural Environmental Research Council (NERC) National Centre for Earth Observation (NCEO), UK.

[D]College of Forest Resources, University of Washington, Mailbox 352100, Seattle, WA, 98195, USA.

[E]Corresponding author. Email: joshua.johnston@canada.ca

Abstract. Byram's fire intensity ($I_{B,tot}$; kW m^{-1}) is one the most important and widely accepted metrics for quantifying wildfire behaviour. Calculation of $I_{B,tot}$ requires measurement of fuel consumption, heat of combustion and rate of spread; existing methods for obtaining these measurements are either inexact or at times impossible to obtain in the field. This paper presents and evaluates a series of remote sensing methods for directly deriving radiative fire intensity ($I_{B,rad}$; kW m^{-1}) using the Fire Radiative Power (FRP) approach applied to thermal infrared imagery of spreading vegetation fires. Comparisons between the remote sensing data and ground-sampled measurements were used to evaluate the various estimates of $I_{B,tot}$, and to determine the radiative fraction (*radF*) of a fire's emitted energy. Results indicate that the $I_{B,tot}$ along an advancing flame front can be reasonably estimated (and agrees with traditional methods of estimation (R^2 = 0.34–0.73)) from appropriately collected time-series of remote sensing imagery without the need for ground sampling or ancillary data. We further estimate that the *radF* of the fire's emitted energy varies between 0.15 and 0.20 depending on the method of calculation, which is similar to previous estimates.

Summary. Methods for remotely measuring Byram's fire intensity with infrared cameras are developed. Experimental data are collected to validate the methods. Results suggest it is possible to using infrared imager to quantify fire intensity.

WF16178

J. M. Johnston et al.

Running header J. M. Johnston et al. / International Journal of Wildland Fire XXX (2017) XXX-XXX

Introduction

Wildfire behaviour is the response of a wildfire to changes in its environment in terms of spread velocity, combustion rate and efficiency, flame length, direction of spread, and depth of burn. Fire intensity, or fire-line intensity, is often considered the most important metric in quantifying wildfire behaviour (Byram, 1959; Alexander 1982). In fire management and research, fire intensity usually refers to Byram's fire intensity ($I_{B,tot}$; kW m^{-1}; Van Wagner 1965; Rothermel and Deeming 1980; Forestry Canada Fire Danger Group 1992), which is the rate of energy (or heat) release per unit time per unit length of the fire front (Byram 1959), and is derived from a linear combination of low heat of combustion, fuel consumption and rate of spread (ROS) (Alexander 1982).

$I_{B,tot}$ and ROS have typically been reported together (Van Wagner 1962, 1965), and are the focus of fire behaviour models (e.g. McArthur 1967; Rothermel 1972; Forestry Canada Fire Danger Group 1992). $I_{B,tot}$ is the conceptual basis for the Canadian Fire Weather Index, which describes the potential fire intensity of a burning forest stand (Van Wagner 1974). $I_{B,tot}$ has also been used in forecasting flame lengths (e.g. Butler *et al*. 2004), determining sufficient safety zones for firefighters (e.g. Butler 2014) and dictating suppression tactics (Flannigan *et al*. 2009; Alexander 2013). The broad-reaching capacity of $I_{B,tot}$ to describe wildfires can best be described by Van Wagner (1977) as containing 'about as much information about a fire's behaviour as can be crammed into one number'.

$I_{B,tot}$ has been routinely calculated based on ROS, fuel consumption and heat of combustion (e.g. McRae *et al*. 1979; Stocks *et al*. 2004; McRae *et al*. 2005), most of which have been applied on experimental fires owing to the difficulties in obtaining fine-resolution data from larger burning areas (e.g. McRae *et al*. 1979; Simard *et al*. 1984; Alexander and Lanoville 1987; Stocks 1987, 1989), where traditional ground-sampling methods often are reduced to a single averaged $I_{B,tot}$ for an entire fire (e.g. Stocks 1987, 1989; Alexander *et al*. 1991). Although certain remote sensing approaches have been proposed (e.g. Smith and Wooster 2005) and tentatively applied (e.g. Zhukov *et al*. 2005; Dickinson *et al*. 2016) in estimating radiative $I_{B,tot}$ ($I_{B,rad}$), none of them have been evaluated against $I_{B,tot}$ values derived from traditional ground-sampling approaches. These approaches in estimating $I_{B,rad}$ are normally based on Fire Radiative Power (FRP) observations, a direct measurement of the radiant energy release rate from fires. Using airborne and satellite remote sensing technologies, FRP can be assessed at landscape to global scales (Kaufman *et al*. 1998; Wooster *et al*. 2003, 2005; Ichoku *et al*. 2008). The temporal integration of FRP gives Fire Radiative Energy (FRE), which describes the total energy released during combustion, and is generally considered proportional to the total fuel consumed (Wooster *et al*. 2005). Notably, where FRP and FRE are used to describe fire energy, only the radiative fraction (*radF*) of $I_{B,tot}$ is quantified, and a correction must be applied to yield actual $I_{B,tot}$.

Although *radF* estimates exist for stationary fires (e.g. Wooster *et al*. 2005; Freeborn *et al*. 2008) and advancing flame fronts (e.g. Kremens *et al*. 2012), this fraction is not well understood with respect to $I_{B,tot}$. Here, we aim to develop and evaluate remote sensing methods for estimating $I_{B,tot}$ without the need for ground-sampled data, for application to very-high-resolution thermal imagery. We compare $I_{B,tot}$ with three estimates of fire intensity derived from FRP- and FRE-based calculations: two are newly developed in the present study and one was previously proposed (Wooster *et al*. 2004; Smith and Wooster 2005). Estimates of *radF* for each method were also derived. Two years of experimental data from a series of moderate-scale burns (~35-m^2 fuel beds) are used in this study. The data from the first year are used to estimate *radF* for each method; experimental data of the second year are used to evaluate the $I_{B,tot}$ prediction ability of each method.

Methodology

Fire intensity estimates

Byram's fire intensity

Byram (1959) proposed three different ways of measuring $I_{B,tot}$ (Eqns 1–3; Table 1), including the popular Byram's Equation (Eqn 1), which is considered the universal $I_{B,tot}$ formula. Unlike Eqn 1, Eqns 2 and 3 have not previously been used owing to technological limitations in field sampling of E_{tot}, the amount of energy released during fuel consumption (FC), and R_{tot}, the heat release rate per unit area, which have now been overcome through remote sensing. For an advancing flame front, $I_{B,tot}$ is not confined to the leading edge of the fire, but is emitted from the full depth of the flaming combustion zone extending inward per unit length of the flame front (Fig. 1). The flame depth (Fig. 1, *d* and Eqn 3) varies extensively with $I_{B,tot}$, ranging from a few centimetres in a low-intensity or back fire to hundreds of metres in situations with extreme fire behaviour (Byram 1959). The flame depth does not include smouldering (solid or glowing) combustion, which may persist for an extended period of time but does not directly contribute to the intensity of the flame front (Alexander 1982). Only fuel consumed during flaming combustion is considered in calculating $I_{B,tot}$ (e.g. Alexander 1982; McRae *et al*. 2005).

If fire spread remains in a steady state over the flame residence time (τ; s), ROS is the flame depth over τ (Eqn 4), which reveals the underlying equivalence of Eqns 1–3 in Eqn 5 (Table 1). However, FRP and FRE are typically given in watts and joules as opposed to the spatially explicit FI_{rad} (kJ m^{-2}) and R_{tot} (kW m^{-2}) as in Eqn 5. Here, we refer to the radiative portion of Etot as FRE density (FRED, kJ m^{-2}; Kremens *et al*. 2012; Hudak *et al*. 2016), and likewise the radiative portion of the R as FRP density (FRPD, kW m^{-2}). Therefore, Eqns 2 and 3 can be adapted to incorporate FRED and FRPD termed the FRED-ROS and the FRPD-Flame Depth (FRPD-FD) methods respectively.

Fire Radiative Energy Density–Rate of Spread (FRED-ROS) method

The FRED-ROS method adapts Eqn 2 as Eqn 6 (Table 1). To describe $I_{B,rad}$ spatially along the fire perimeter, FRED is measured for each pixel along the perimeter. From a temporal perspective, FRED requires enough observations to properly characterise the fluctuations in FRPD over time. Eqn 5 can then

Publisher: CSIRO; Journal: WF:International Journal of Wildland Fire
Article Type: research-article; Volume: ; Issue: ; Article ID: WF16178
DOI: 10.1071/WF16178; TOC Head:

be restructured as Eqn 7 (Table 1), where ROS represents the previous time step normal to the perimeter (e.g. Paugam *et al*. 2013, Fig. 2*a*). When applied to high-resolution imagery, Eqn 7 is rasterised by interpolating the time series of FRPD at each pixel and integrating over the time domain of τ. $I_{B,rad}^{\text{FRED-ROS}}$ is mapped to each perimeter pixel where ROS is available for computing Eqn 6.

Fire Radiative Power Density–Flame Depth (FRPD-FD) method

This FRPD-based method is rooted directly in Eqn 3, with the parameters adapted as in Eqn 8 (Table 1), where *d* is the length of the normal extending from a perimeter pixel to the rear of the flame depth, computed in raster cells using Pythagorean theorem scaled by the pixel resolution (Eqn 8). R_{rad} is computed as the total FRPD for all pixels intersected by *d* at that point (Fig. 2*b*).

As in the assumptions of Eqn 5, if the flame front is in a steady state, integrating the time series of FRPD at a pixel over τ (Eqn 7) is equivalent to integrating the FRPD along the depth of the flame front (Eqn 8), whereas the spatial distribution of the flame depth is inherently connected through Eqn 4; thus, these methods are conceptually interchangeable only during steady-state burning conditions. However, a steady state is only required for Eqns 1 and 2, whereas Eqn 3 (and the FRPD-FD method) is valid in both steady and unsteady conditions (Dold *et al*. 2009; Dold 2010). As such, Eqn 5 is expected to hold only where a steady state exists. Therefore, Eqns 1, 2 and 3 will not always produce an identical output; in fact, deviation from one another may indicate an unsteady state.

Fire Radiative Power–Flame Front Length (FRP-FFL) method

Smith and Wooster (2005) proposed a separate method to convert FRP into an estimate of $I_{B,rad}$ averaged over the flame front length (Eqn 9, Table 1, Fig. 2*c*).

Experimental design and protocol

In order to assess the ability of the three methods for estimating $I_{B,rad}$ from thermal remote sensing data, we conducted 21 experimental fires during 2013 and 2014. Data collected included detailed fuel moisture, heat of combustion, fuel loading and consumption measurements. Near-vertically viewing tower-mounted thermal infrared imagers were deployed, and in 2014, a thermocouple grid was deployed in the fuel bed for independent ROS calculation.

Experimental location and burn platform layout

Both experimental campaigns were conducted at the Canadian Forest Service's Rose Experimental Burn Station (near Thessalon, Ontario, Canada). At this open-air facility, a burn platform was constructed at the base of a 30-m scaffold tower on which the thermal imaging cameras were mounted. To ensure that no ash was lost post burn, a layer of 12 'fire-proof' 1.27-cm-thick type 'M' marinite boards were used to form the base of the burn platform, arranged into three rows of four (1.21 × 2.43-m) panels (Fig. 3*a*, *d*). In 2014, the junction points of the panels were used for establishing a grid of 20 K-type 24-gauge (0.56-mm diameter) thermocouples, with edge thermocouples inset 0.3 m into the panel to ensure flame contact (Fig. 3*d*).

Infrared imaging

In 2013 and 2014, two different infrared imagers where used (Table 2). Orientation of the tower, burn platform and camera positions for the moderate-scale experimental burns from which the measures of $I_{B,tot}$ were taken are shown in Fig. 4.

Fuels

All fuels in this experiment consisted of dried longleaf pine (*Pinus palustris*s) needles. The uniformity of the needles and their homogeneous arrangement across the burn platform permitted a high level of experimental control. Fuel parameters (Table 3) were determined by direct measurement of random destructive samples taken throughout the experimentation.

Burn protocol

The weighed fuel was loosened and evenly distributed by row of the platform (Fig. 3*a*). A standard forestry drip torch was used to ignite the fuel beds. For all burns, ignition was conducted along the west edge of the platform and consisted of a series of tightly spaced ignition lines ~0.5 m into the fuel bed perpendicular to the edge. Given the short (7.34 m) distance available for spread, this ignition pattern minimised the acceleration stage of fire growth (Fig. 3). Burns were allowed to smoulder past the stage of flaming combustion; however, in all cases combustion had ended within ~5 min of flame front passage, with minimal smouldering (owing to fuel structure and moisture). Once each burn was complete, all residual ash was immediately collected and weighed by row (to prevent loss due to wind, or excessive smouldering).

Data collection

Data collection

Fuel beds varied among burns in terms of fuel loading, fuel depth and fuel moisture content (owing to atmospheric humidity; Table 4). The heat of combustion was calculated using an oxygen bomb calorimeter for three randomly selected samples ranging between 0.55 and 0.76 g.

Once the fuel was laid out, fuel depth measurements were taken at three random locations within each of the ten accessible panels along the perimeter of the burn platform, providing 30 measurements per burn. Destructive fuel samples were taken within 10 min of ignition from each perimeter panel to determine gravimetric moisture content (GMC, % dried mass; Table 4).

Thermal infrared (TIR) imaging was performed through the entirety of each burn. In 2014, thermocouple outputs were logged using a series of data loggers at a rate of 2 Hz.

Data processing

Estimating $I_{B,tot}$ *with Eqn 1*

For $I_{B,tot}$ estimation, the low heat of combustion was calculated by removing the latent heat of vaporisation and making reductions separately for each burn based on the fuel GMC (Alexander 1982; Table 5). Fuel consumption values were computed for each burn by calculating the difference between pre- and post-burn dry fuel loads (Table 5). ROS values were derived from the TIR imagery taken from the fixed camera positions viewing near vertically from atop the 30-m tower (Table 5). The low heat of combustion, FC and ROS values were used to compute $I_{B,tot}$ in Eqn 1 for each burn platform panel, which was then generalised to describe $I_{B,tot}$ by row and by burn as required using median values.

Estimating $I_{B,tot}$ *with FRP, FRPD and FRED*

Thermal infrared preprocessing. In order to enable spatial measurements of ROS and flame dimensions, spatially explicit data were required. All infrared imagery was georeferenced using a direct linear transform (DLT; a linear remapping of pixels into a uniform planar field), with output remapped to a single uniform pixel size across the full burn extent (see Pastor *et al*. 2006; Paugam *et al*. 2013). Corners of the burn platform were used as ground control points (GCPs) and measured to ±0.005-m uncertainty using a high-precision laser scanner. Prior to applying the DLT to the imagery, the pixel brightness temperatures (K) were converted to spectral radiance units (Watts meter–2 steradian–1 micrometer–1; W m^{-2} sr^{-1} μm^{-1}) using the camera's spectral response function and the inverse Planck function, because the Planck function is strongly non-linear in the mid-wave infrared (MWIR) across fire temperature ranges (e.g. Wooster *et al*. 2005; Johnston *et al*. 2014). This step was necessary because calculation of FRP was performed after the DLT to conserve energy during the transformation. In applying the DLT, the spatial resolution of the geocorrected imagery was degraded with the new pixel radiances calculated as the area-weighted average of their subpixel constituents (e.g. Dozier 1981), and then the radiance values were converted back to brightness temperatures for further analysis. For all data, the final uniform pixel resolution was 0.13 m.

ROS calculation

The approach developed by Paugam *et al*. (2013) was also used to calculate ROS from the resampled TIR imagery for both the 2013 and 2014 burns. Owing to the far smaller pixel size in the present study compared with that of Paugam *et al*. (2013), to maximise agreement of the TIR image-derived fire arrival times at a location with those derived from the thermocouple measurements, the brightness temperature (BT) threshold indicating the time of arrival was increased from the assumed 650 K (Paugam *et al*. 2013) to 773 K. For the ROS calculation made using the fire arrival time map, imagery was sampled every 5–10 s (with higher-frequency sampling used for faster-spreading fires, Table 5). Notably, ROS is not available for all perimeter pixels as the normal vector occasionally exits the burn platform in places rather than intersecting another perimeter. At every level of sampling, these ROS data are typically skewed to higher values (as discussed in McRae *et al*. 2005) and therefore the median values are reported by row.

For the 2014 burns, data from the thermocouple (TC) grid were also used to estimate fire arrival times (based on a TC temperature threshold of 573 K; Wotton *et al*. 2012), supporting an independent $I_{B,tot}$ calculation. Arrival times were used in groups of three to compute rate and direction of spread using the approach of Simard *et al*. (1984). For the final analysis, these results were generalised to the row level.

FRP calculation

FRP was computed using the MWIR radiance method of Wooster *et al*. (2003, 2005), with the FRP factors tailored to the spectral response function of each TIR camera used as detailed in Wooster *et al*. (2005). FRP was produced using the georeferenced imagery in units of Watts pixel^{-1}, and converted to FRPD (kW m^{-2}) as needed by multiplication by the pixel area. FRED maps in kilojoules pixel^{-1} (and kJ m^{-2}) were produced by temporal integration of FRPD for each pixel.

Infrared fire intensity measurement

Measurement of $I_{B,rad}$ was conducted distinctly for each of the methods tested here; as a result, $I_{B,rad}$ values from different methods are not necessarily equivalent to one another (Table 6). For example, owing to the limited fuel bed width (4.88 m), sampling FRPD along the local normal vectors for the FRPD-FD method resulted in numerous vector intersections and resampling of FRPD pixels. To mitigate this issue, two points were selected at opposite ends of the flame front and a single normal for each time step was generated, resulting in parallel flame depth vectors.

Analysis

TIR and ground-sampled data from Row 1 of the burns (Fig. 3*a*) were not analysed because they were contaminated by the drip torch fuel used for ignition. For each method, we used the 2013 dataset to estimate the *radF* as the ratio of $I_{B,rad}$ to $I_{B,tot}$, but reserved the 2014 dataset for validation. Byram (1959) provides an estimate of ~10–20% as general target range of *radF*. More recently, both Wooster *et al*. (2005) and Freeborn *et al*. (2008) measured *radF* from laboratory-scale stationary fires as 14 and 11% (respectively) when fuel moisture is considered (as it is in the results of the present study (Kremens *et al*.

2012; Smith *et al*. 2013)). Unlike earlier studies, Kremens *et al*. (2012) examined open-air spreading flame fronts and found the *radF* to be somewhat higher, at 17%. The difference between stationary and spreading fires is significant in terms of flame front structure and the spatiotemporal distribution of flaming and smouldering fuels. This difference has a significant effect on *radF* and depends on correct sampling of $I_{B,rad}$. The range suggested by Byram and the measurements of Kremens *et al*. (2012) were used as reference in evaluating our results. Here, the *radF* is an instantaneous comparison of $I_{B,rad}$ with $I_{B,tot}$ and is different from other calculations that typically compare total radiant energy with total energy released during combustion (e.g. Wooster *et al*. 2005; Freeborn *et al*. 2008; Kremens *et al*. 2012). The 2014 dataset was used further to compare the *radF* corrected methods with the ground-sampled $I_{B,tot}$ (in Eqn 10, Table 1). In both comparisons, linear regression analysis of $I_{B,rad}$ (or $I_{B,tot}$ in 2014) vs $I_{B,tot}$ was used. In the direct $I_{B,tot}$ with $I_{B,tot}$ comparisons, linear regression results were examined to determine the significance of their deviation from the line of perfect agreement (LPA) as in Legg *et al*. (2007); the *R* programming language was used for all statistical analysis.

Testing and determining radiative fractions

Analysis of FRP- and FRPD-based methods. Median values of $I_{B,rad}^{\text{FRPD-FD}}$ and $I_{B,rad}^{\text{FRP-FFL}}$ for each row were compared with $I_{B,tot}$ (Eqn 1), to assess each method's ability to describe $I_{B,rad}$. The fastest-moving fires were not analysed because the fire reached the end of the fuel bed while the ignition line was still flaming (e.g. 12 June 2013 Burn 1, and 18 June 2013 Burn 2), preventing the full flame depth from developing.

Analysis of FRED-ROS method. The FRED-ROS method was not directly evaluated against $I_{B,tot}$ as the ROS of Paugam *et al*. (2013) was used by both the $I_{B,tot}$ and $I_{B,rad}^{\text{FRED-ROS}}$ calculations, resulting in a lack of complete independence in the data. Also, it is not desirable to sample ROS using independent methods as this introduces error where the ROS outputs do not perfectly agree (e.g. Johnston 2016). However, because both the FRED-ROS and Eqn 2 include ROS as a linear factor, the FRED-ROS method was evaluated by comparing the remaining terms in Eqns 2 and 6.

Statistical analysis of radF. Data with respect to burn, row, ROS, FC and GMC were analysed for each sample of *radF* from the various FI_{rad} methods. For each $I_{B,rad}$ method, backward stepwise linear regression analysis was performed, using all these parameters and their interactions as predictors of *radF*. Additionally, mixed-effect model analysis was conducted where $I_{B,rad}$ method, ROS, FC and GMC were treated as fixed effects, and burn and row were treated as random effects in predicting *radF*.

Validation of $\mathrm{I}_{\mathrm{B,tot}}$ *methods*

The FRPD-FD and FRED-ROS methods were evaluated using the 2014 data by applying Eqn 10 to $I_{B,rad}^{\text{FRPD-FD}}$ and $I_{B,rad}^{\text{FRED-ROS}}$ and the *radF* calculated with the 2013 data to yield complete $I_{B,tot}$, which was compared with ground-sampled $I_{B,tot}$. This validation was not attempted with the FRP-FFL owing to the limited success in the initial analysis (see *Results*).

Notably, the *radF* (Figs 6–8) distributions range from 0.1 to 0.6; attempts to model *radF* based on additional experimental data were not significant (see *Results*). In the context of the present study, fixed exemplar *radF* were applied in an attempt to determine which fraction best suits these experimental conditions.

The FRPD-FD method was evaluated using the derived *radF* of 0.26 (median of the distribution in Fig. 7*d*), 0.24 (the regression coefficient in Fig. 7*c*), and 0.17 (the value used in the FRED-ROS validation). Notably, *radF* are linear scalars of FI_{rad}, so they have no effect on R^2 or P values for each trial (Fig. 9).

The FRED-ROS method was evaluated using the estimated *radF* 0.21 (median in Fig. 8), 0.17 (the regression coefficient of the non-independent comparison) and 0.15 (near lower bound of the range suggested by Kremens *et al.* 2012). Fig. 10 shows the results of the comparison of these data with the 2014 data, using the $I_{B,tot}$ produced with the IR ROS, which suffered from the same lack of independence that interfered with the initial evaluation. This evaluation was then repeated using the TC ROS for $I_{B,tot}$ (Fig. 11).

Results

FRP- and FRPD-based methods of $\mathrm{FI}_{\mathrm{rad}}$ *measurement*

The linear regression shows a significant relationship between $I_{B,tot}$ and the FRP-FFL method by row of the burn platform (Fig. 6*a*); however, the relationship is not stronger than that of relating FRP directly to $I_{B,tot}$ (Fig. 5) and it showed no advantage in predicting $I_{B,rad}$. The *radF* of this method has a mean value of ~0.10, with a broad range (Fig. 6*b*), indicating a lack in stability. A second iteration of this method was executed with FRP limited to the flaming pixels, but showed no significant improvement (Fig. 6*c*, *d*), suggesting the length measure (which is constrained by plot size) may be the limiting factor rather than the FRP sample area.

Linear regression between $I_{B,tot}$ and the FRPD-FD method by row using the 773 K arrival and 773 K flame termination thresholds showed no significance (Fig. 7*a*). Similarly, the *radF* distribution is very unstable (Fig. 7*b*). The linear regression between $I_{B,tot}$ and the FRPD-FD method by row using the 773 K arrival and 700 K flame termination thresholds (Fig. 7*c*) is significant, and superior to that of the FRP-FFL and FRP comparisons. The mean fraction derived from the *radF* distribution is 0.29 (Fig. 7*d*).

FRED-ROS method of $\mathrm{FI_{rad}}$ *measurement*

Direct comparison of the FRED-ROS method with $I_{B,tot}$ is significant ($R^2 = 0.97$, $P < 0.0001$), but misleading owing to the lack of independence in ROS; however, the regression coefficient (0.17) is valuable as a potential *radF* value. Alternatively, comparison of FRED with E_{tot} (from Eqn 2) is also significant (Fig. 8*a*) and the *radF* takes on a fairly normal distribution (Fig. 8*b*), with a mean of 0.21 (s.d. 0.04).

Results of statistical analysis of radF

The linear regression analysis of *radF* with all predictors and their interactions for the FRED-ROS method was significant (but not for the other two methods[A]) and the backward stepwise approach revealed that GMC is a weak predictor of *radF* (adj. $R^2 = 0.07$, $P = 0.04$). The mixed model analysis of *radF* including method as a fixed effect and the random effects of burn and row was not significant ($P >$ 0.05 for all predictors).

Direct estimation of $\mathrm{I_{B,tot}}$ *using the 2014 dataset*

The FRPD-FD method was evaluated as a predictor of $I_{B,tot}$ using *radF* corrections. For the *radF*s tested (0.26, 0.24 and 0.17), the regressions were significant (Fig. 9). However, the agreement was somewhat weak (Fig. 9), and the deviation from the LPA was not significant for all *radF*s tested (Table 7). Notably, when validating the FRPD-FD method with the 0.17 *radF*, the *t*-score is negative (Table 7), indicating that this model overestimates $I_{B,tot}$ (Fig. 9*c*), which could be attributed to an underestimation of the *radF*. This suggests the ideal *radF* lies between 0.17 (c) and 0.24 (b).

When evaluating the FRED-ROS method as predictor of $I_{B,tot}$ with *radF* corrections, all fractions tested were significant (Fig. 10). All the regressions were significant while using independent TC ROS for the ground-sampled $I_{B,tot}$ in the tests (Fig. 11). As shown in Fig. 11, given the much lower R^2 (0.34), the LPA remains in the 95% confidence interval (CI) for all three *radF* values, and the deviation from the LPA was not significant in this case for all *radF*s tested (Table 7). Notably, the *radF* of 0.15 produces the most accurate results for the FRED-ROS method where the ROS was not independently calculated (Fig. 10). With the lack of specific results in comparing this method with $I_{B,tot}$ with independent ROS (where the correlation is much weaker), and the certainty of the results from the comparison in Fig. 10, it is probable that the *radF* of 0.15 (Fig. 10*c*) is best suited for the FRED-ROS method at this scale.

Publisher: CSIRO; Journal: WF:International Journal of Wildland Fire
Article Type: research-article; Volume: ; Issue: ; Article ID: WF16178
DOI: 10.1071/WF16178; TOC Head:

Discussion

This study suggests that with high-spatial-resolution TIR imagery, the FRPD-FD is superior to the FRP-FFL method in estimating FI_{rad} from a single image. The major difference is that the FRPD-FD method samples $I_{B,tot}$ at individual positions along the flame front (Byram 1959; Eqn 3), producing unique estimates of $I_{B,rad}$ at each point, whereas the FRP-FFL method averages $I_{B,rad}$ across the full length of the flame front. Both methods are quite sensitive to how the distance measures are calculated, though *d* measurements (e.g. Fig. 12) vary significantly along the flame front, FFL offers a single value for each image. The FRPD-FD method only functions when the flame depth is correctly measured (e.g. Fig. 7), and the FRP-FFL method may be limited by the lack of a complete flame front length (i.e. a fire perimeter that encircles the fire area) as the FRP sampling zone does not affect its performance (Fig. 6). Additional assessment at larger scales is required to determine if this is indeed the limiting factor on the FRP-FFL method.

Even without ROS, the FRED-ROS performs strongly compared with the FRP and FRPD methods. The *radF* (0.21 ± 0.04, Fig. 8*b*) is similar to the upper bound proposed by Byram (1959), and overlaps with that of more recent work (e.g. 0.17 ± 0.03; Kremens *et al*. 2012).

In the case of the FRED-ROS method, GMC did show borderline significance (adj. $R^2 = 0.07$, $P = 0.04$) in predicting *radF*. This result is in agreement with recent studies that found a connection between fuel moisture and the FRP to FC relationship (e.g. Smith *et al*. 2013), and is not surprising given that low heat of combustion is determined in part by GMC (Alexander 1982). It is probable that variability in *radF* is better explained by parameters not tested here, such as heterogeneity of soot distribution, vertical flame depth and other geometric properties, because flame emissivity is largely controlled by the depth of the viewing path (Johnston *et al*. 2014).

In both cases, when the FRED-ROS and the FRPD-FD methods were compared with independent ground-sampled $I_{B,tot}$ datasets, an R^2 of ~0.3–0.4 was observed. The relatively weak R^2 here can be partly attributed to the imperfect agreement between the independent ROS methods being used (R^2 = 0.42–0.77). It may also be attributed to the application of Eqns 1 and 2 where the fires are periodically not in a steady state (Dold *et al*. 2009; Dold 2010), which would also affect the evaluation of the FRPD-FD method as it is compared with Eqn 1. That being said, in both cases, the regression coefficient of the linear fit was much closer to the LPA and prediction bias was lowered when *radF* was below 20% (lower than the value estimated from the data herein). Therefore, for these data, the true *radF* of FRP-driven $I_{B,tot}$ measurements may indeed fall within the range suggested by Byram (1959) of 10–20% and those measured by Wooster *et al*. (2005), Freeborn *et al*. (2008) and Kremens *et al*. (2012) (~14, ~11 and ~17% respectively).

A key assumption in applying these methods and in deriving the *radF* is that FRP accurately characterises *radF* emissions. FRP calculations apply the Stefan–Boltzmann law to determine total radiant exitance assuming that fire emissions obey Lambert's cosine law (e.g. Wooster *et al*. 2003). However, radiant fire energy has been found to vary with observation angle (e.g. Freeborn *et al*. 2008; Frankman *et al*. 2013), and as such the Lambertian assumption may not be strictly accurate. This potential error has also been acknowledged in the context of measuring radiation from flame fronts (Kremens *et al*. 2012). Therefore, the *radF* found in the present study may not be identical where flame structure and viewing angles differ substantially from the present conditions. A comprehensive physical model for *radF* may overcome these restrictions.

In applying the FRED-ROS method, FRPD should only be integrated over τ to prevent the inclusion of smouldering energy. This is not always practical in validation studies, as fuel consumption values available from ground sampling often also include some smouldering FC (Alexander 1982). Subsequently, when comparing Eqn 7 outputs with ground-sampled values, the time domain should reflect the time gap before FC sampling, and when applied to describe true $I_{B,tot}$ integration should be limited to τ. In this study, FRPD was integrated over the full time series; however, given the fuels and experimental conditions, virtually no smouldering combustion was observed.

The FRED-ROS method has the advantage that it includes the most temporally unstable inputs to $I_{B,tot}$ (ROS) directly, providing a complete description of fire behaviour along the perimeter (Fig. 13). However, this advantage also demands very high-temporal-resolution imagery, which is frequently unavailable. This method is also limited by the assumption that the flame front is travelling at a steady state between observations; consequently as the temporal resolution of FRPD sampling is reduced, the uncertainty increases.

The FRPD-FD method provides an instantaneous measurement of $I_{B,tot}$ but is not limited by frequency of data observations and assumptions of a steady state. However, it does lack an explicit reference to ROS, which is desirable to report alongside $I_{B,tot}$ (Van Wagner 1965; Alexander 1982; McRae *et al*. 2005); if ROS is of interest, additional assumptions may be required to evoke Eqn 4. Eqn 8 is limited by the quality of the measurement of *d*. Highly accurate flame depth measurements are required and it is difficult to assess the effect of all potential factors (e.g. smoke plume absorption) on the temperature thresholds for determining *d*. At the same time, for imagery with larger pixel areas, it is necessary to estimate subpixel fire characteristics to implement this method (e.g. effective fire area by bispectral analysis; Dozier 1981; Gilgio and Kendall 2001), to estimate the depth of the flame front. The correctness of such an application would be suspect until further testing is conducted.

Conclusion

In this study, three potential methods for estimating $I_{B,tot}$ directly from TIR imagery were evaluated. This study has shown that it is possible to measure $I_{B,tot}$ on moderate scale for actively spreading flame fronts at a fine resolution (0.13 m), using only TIR remote sensing. We demonstrated that Byram's *other* equations (Eqns 2 and 3) are not only applicable to open-air fires, but may be more easily applied in the field than Eqn 1.

The FRED-ROS and FRPD-FD methods successfully predicted $I_{B,tot}$ under data-rich conditions. Though their functionality is not necessarily conclusive based solely on the agreement they exhibited with ground-sampled data, these reservations are offset by their physical basis in Eqns 2 and 3, and under steady-state conditions should be considered equally acceptable methods of estimating $I_{B,tot}$ alongside Byram's Equation (Eqn 1). Our evaluation also suggests that the *radF* of these fires may be within the ~10–20% range suggested by Byram (1959). Whether the effectiveness of these methods at larger scales and whether the *radF* will remain in a similar range when flames increase in size (and therefore change their optical properties) requires further investigation. The effect of increasing pixel sizes and time intervals between observations also remains unknown and need to be investigated further. Additionally, development of a physical model for the *radF* of $I_{B,tot}$ capable of varying with parameters such as viewing angle, flame structure and optical properties may broaden applications of these methods in the future. Pending further evaluation, it is possible that when used together, disagreement of the FRED-ROS and FRPD-FD methods may indicate deviation from steady-state burning conditions, indicating a potential hazard for fire managers.

Acknowledgements

The authors would like to thank John Studens, Alison Newbery, Alan Cantin, Dr Dan Thompson, Natasha Jurko, Dr Bruce Main, François Gonard and Dr Mike Wotton for their assistance in the execution of the experimental burns. We would like to thank Dr G. Matt Davies, Dr Rachel Gaulton and Professor Mike Flannigan for their insightful comments on the early manuscript, and the reviewers for their constructive input. Critical support for this project was provided by the Canadian Space Agency and the European Space Agency. Martin Wooster's work is supported by the UK Natural Environmental Research Council (NERC) and NERC grant NE/J014060/1 supported some of the work described herein. The NERC Geophysical Equipment Facility (NERC-GEF) is also acknowledged for loan and training related to use of the terrestrial laser scanner.

References

<jrn>Alexander ME (1982) Calculating and interpreting forest fire intensities. *Canadian Journal of Botany* **60**, 349–357. doi:10.1139/b82-048</jrn>

<edb>Alexander ME (2013) Fire management applications of wildland fire behaviour knowledge. In ‘Fire on Earth: an Introduction’. (Eds AC Scott, DMJS Bowman, WJ Bond, SJ Pyne, ME Alexander) 373-391 (Wiley Blackwell: Hoboken, NJ, USA)</edb>

<conf>Alexander ME, Lanoville RA (1987) Wildfires as a source of fire behavior data: a case study from Northwest Territories, Canada. In ‘Ninth Conference on Fire and Forest Meteorology’, 21–24 April 1987, San Diego, CA, USA. (American Meteorological Society: Boston, MA, USA)</conf>

<bok>Alexander ME, Stocks BJ, Lawson BD (1991) Fire behavior in black spruce–lichen woodland: the Porter Lake project. Forestry Canada, Northwest Region, Northern Forestry Centre, Edmonton, Alberta. Information Report NOR-X-310..</bok>

<jrn>Butler B (2014) Wildland fire fighter safety zones: a review of past science and summary of future needs. *International Journal of Wildland Fire* **23**, 295–308. doi:10.1071/WF13021</jrn>

<jrn>Butler B, Finney M, Andrews P, Albini F (2004) A radiation-driven model for crown fire spread. *Canadian Journal of Forest Research* **34**, 1588–1599. doi:10.1139/x04-074</jrn>

<edb>Byram GM (1959) Combustion of forest fuels. In ‘Forest Fire: Control and Use’. (Ed. KP Davis) pp. 61–89. (McGraw-Hill: New York, NY, USA)</edb>

<jrn>Dickinson MB, Hudak AT, Zajkowski T, Loudermilk EL, Schroeder W, Ellison L, Kremens RL, Holley W, Martinez O, Paxton A, Bright BC, O’Brien JJ, Hornsby B, Ichoku C, Faulring J, Gerace A, Peterson D, Mauceri J (2016) Measuring radiant emissions from entire prescribed fires with ground, airborne and satellite sensors – RxCADRE 2012. *International Journal of Wildland Fire* **25**, 48–61. doi:10.1071/WF15090</jrn>

<conf>Dold JW (2010) Vegetation engagement in unsteady fire spread. In ‘VI International Conference on Forest Fire Research’, Coimbra, Portugal. (Ed. DX Viegas)</conf>

<conf>Dold JW, Zinoviev A, Leslie E (2009) Fire intensity accumulation in unsteady fireline modelling. In ‘Sixth Mediterranean Combustion Symposium’, 7 June–12 June 2009, Corsica.</conf>

<jrn>Dozier J (1981) A method for satellite identification of surface temperature fields of subpixel resolution. *Remote Sensing of Environment* **11**, 221–229. doi:10.1016/0034-4257(81)90021-3</jrn>

<jrn>Flannigan MD, Krawchuk MA, de Groot WJ, Wotton BM, Gowman LM (2009) Impacts of changing climate for global wildland fire. *International Journal of Wildland Fire* **18**, 483–507. doi:10.1071/WF08187</jrn>

<other>Forestry Canada Fire Danger Group (1992) Development and structure of the Canadian Forest Fire Behavior Prediction System. Forestry Canada, Science and Sustainable Development Directorate, Information Report ST-X-3. (Ottawa, ON, Canada)</other>

<jrn>Frankman D, Webb BW, Butler BW, Jimenez D, Forthofer JM, Sopko P, Shannon KS, Hiers JK, Ottmar RD (2013) Measurements of convective and radiative heating in wildland fires. *International Journal of Wildland Fire* **22**, 157–167. doi:10.1071/WF11097</jrn>

<jrn>Freeborn P, Wooster MJ, Hao WM, Ryan CA, Nordgren BL, Baker SP, Ichoku C (2008) Relationships between energy release, fuel mass loss, and trace gas and aerosol emissions during laboratory biomass fires. *Journal of Geophysical Research* **113**, D01301. doi:10.1029/2007JD008679</jrn>

Giglio, L, Kendall, JD (2001) Application of the Dozier retrieval to wildfire characterization: a sensitivity analysis. Remote Sensing of Environment 77, 34-49.

<jrn>Hudak AT, Dickinson MB, Kremens RL, Bright BC, Loudermilk EL, O'Brien JJ, Hornsby B, Ottmar RD (2016) Measurements relating fire radiative energy density and surface fuel consumption – RxCADRE 2011 and 2012. *International Journal of Wildland Fire* **25**, 25–37. doi:10.1071/WF14159</jrn>

<jrn>Ichoku C, Giglio L, Wooster MJ, Remer LA (2008) Global characterization of biomass-burning patterns using satellite measurements of fire radiative energy. *Remote Sensing of Environment* **112**, 2950–2962. doi:10.1016/j.rse.2008.02.009</jrn>

<bok>Johnston JM (2016) Infrared remote sensing of fire behaviour in Canadian wildland forest fuels. PhD thesis, King's College London.</bok>

<jrn>Johnston JM, Wooster MJ, Lynham TJ (2014) Experimental confirmation of the MWIR and LWIR greybody assumption for vegetation fire flame emissivity. *International Journal of Wildland Fire* **23**, 463–479. doi:10.1071/WF12197</jrn>

<jrn>Kaufman Y, Kleidman R, King M (1998) SCAR-B fires in the tropics: properties and remote sensing from EOS-MODIS. *Journal of Geophysical Research* **103**, 31955–31968. doi:10.1029/98JD02460</jrn>

<jrn>Kremens RL, Dickinson MB, Bova AS (2012) Radiant flux density, energy density, and fuel consumption in mixed-oak forest surface fires. *International Journal of Wildland Fire* **21**, 722–730. doi:10.1071/WF10143</jrn>

<bok>Legg C, Davies M, Kitchen K, Marno P (2007) A fire danger rating system for vegetation fires in the UK: The FireBeaters Project Phase 1 Final Report. The University of Edinburgh and The Met Office. (Edinburgh, UK).</bok>

<bok>McArthur AG (1967) Fire behaviour in eucalypt forests. Commonwealth of Australia, Forestry and Timber Bureau Leaflet 107. (Canberra, ACT)</bok>

<bok>McRae DJ, Alexander ME, Stocks BJ (1979) 'Measurement and Description of Fuels and Fire Behavior on Prescribed Burns: a Handbook.' (Great Lakes Forest Research Centre: Sault Ste Marie, ON, Canada).</bok>

<jrn>McRae DJ, Jin J-Z, Conard SG, Sukhinin AI, Ivanova GA, Blake TW (2005) Infrared characterization of fine-scale variability in behaviour of boreal forest fires. *Canadian Journal of Forest Research* **35**, 2194–2206. doi:10.1139/x05-096</jrn>

<jrn>Pastor E, Àgueda A, Andrade-Cetto J, Muñoz M, Pérez Y, Planas E (2006) Computing the rate of spread of linear flame fronts by thermal image processing. *Fire Safety Journal* **41**, 569–579. doi:10.1016/j.firesaf.2006.05.009</jrn>

<jrn>Paugam R, Wooster MJ, Roberts G (2013) Use of handheld thermal imager data for airborne mapping of fire radiative power and energy and flame front rate of spread. *IEEE Transactions on Geoscience and Remote Sensing* **99**, 1–15.</jrn>

<other>Rothermel RC (1972) A mathematical model for predicting fire spread in wildland fuels. USDA Forest Service, Intermountain Forest and Range Experiment Station, Research Paper INT-115. (Ogden, UT, USA)</other>

<bok>Rothermel R, Deeming J (1980) Measuring and interpreting fire behavior for correlation with fire effects. USDA Forest Service, Intermountain Forest and Range Experiment Station, (Ogden, UT, USA), General Technical Report INT-93.</bok>

<jrn>Simard A, Eenigenburg J, Adams K, Nissen R, Jr, Deacon A (1984) A general procedure for sampling and analyzing wildland fire spread. *Forest Science* **30**, 51–64.</jrn>

<jrn>Smith AMS, Wooster MJ (2005) Remote classification of head and backfire types from MODIS fire radiative power and smoke plume observations. *International Journal of Wildland Fire* **14**, 249–254. doi:10.1071/WF05012</jrn>

<jrn>Smith AMS, Tinkham WT, Roy DP, Boschetti L, Kremens RL, Kumar SS, Sparks AM, Falkowski MJ (2013) Quantification of fuel moisture effects on biomass consumed derived from fire radiative energy retrievals. *Geophysical Research Letters* **40**, 6298–6302. doi:10.1002/2013GL058232</jrn>

<jrn>Stocks BJ (1987) Fire behaviour in immature jack pine. *Canadian Journal of Forest Research* **17**, 80–86. doi:10.1139/x87-014</jrn>

<jrn>Stocks BJ (1989) Fire behaviour in mature jack pine. *Canadian Journal of Forest Research* **19**, 783–790. doi:10.1139/x89-119</jrn>

<jrn>Stocks BJ, Alexander ME, Wotton BM, Stefner CN, Flannigan MD, Taylor SW, Lavoie N, Mason JA, Hartley GR, Maffey ME, Dalrymple TW, Blake TW, Cruz MG, Lanoville RA (2004) Crown fire behaviour in a northern jack pine–black spruce forest. *Canadian Journal of Forest Research* **34**, 1548–1560. doi:10.1139/x04-054</jrn>

<bok>Taylor SW, Pike RG, Alexander ME (1997) Field guide to the Canadian Forest Fire Behavior Prediction (FBP) System. Northern Forestry Centre. (Edmonton, AB, Canada), Special Report 11.</bok>

<jrn>Van Wagner C (1962) On the value of a numerical concept of fire intensity. *Pulp & Paper magazine of Canada, Woodland review.* **63**, 458–459.</jrn>

<eref>

<jrn>Van Wagner CE (1965) Describing forest fires – old ways and new. *Forestry Chronicle* **41(3), 301-305**.</jrn>

<bok>Van Wagner CE (1974) Structure of the Canadian Forest Fire Weather Index. Department of the Environment, Canadian Forestry Service, Publication number 1333. (Ottawa, ON, Canada)</bok>

<jrn>Van Wagner CE (1977) In readers' forum. *Fire Technology* **13**, 349–350. doi:10.1007/BF02319734</jrn>

<jrn>Wooster MJ, Zhukov B, Oertel D (2003) Fire radiative energy for quantitative study of biomass burning: derivation from the BIRD experimental satellite and comparison to MODIS fire products. *Remote Sensing of Environment* **86**, 83–107. doi:10.1016/S0034-4257(03)00070-1</jrn>

<edb>Wooster MJ, Perry G, Zhukov B, Oertel D (2004) Estimation of energy emissions, fireline intensity and biomass consumption in wildland fires: a potential approach using remotely sensed fire radiative energy. In ‘Spatial Modelling of the Terrestrial Environment’. (Eds R Kelly, N Drake, S Barr) 177-198 (Wiley: London, UK)</edb>

<jrn>Wooster MJ, Roberts G, Perry GLW, Kaufman YJ (2005) Retrieval of biomass combustion rates and totals from fire radiative power observations: FRP derivation and calibration relationships between biomass consumption and fire radiative energy release. *Journal of Geophysical Research* **110**, D24311. doi:10.1029/2005JD006318</jrn>

<jrn>Wotton B, Gould J, McCaw W, Cheney N, Taylor S (2012) Flame temperature and residence time of fires in dry eucalypt forest. *International Journal of Wildland Fire* **21**, 270–281. doi:10.1071/WF10127</jrn>

<conf>Zhukov B, Oertel D, Lorenz E, Ziman Y, Csiszar I (2005) ‘Comparison of Fire Detection and Quantitative Characterization by MODIS and BIRD, 31st International Symposium on remote sensing of Environment Proceedings.’ June 20-24, 2005, Saint Petersburg, Russia.</conf>

Received 20 September 2016, accepted 10 May 2017

Table 1. Equation summary

Parameters: $I_{B,tot}$, Byram's fire intensity (kW m^{-1}); H_{tot}, low heat of combustion (kJ kg^{-1}); w, fuel consumption (kg m^{-2}); r = ROS, rate of spread (m s^{-1}); E_{tot}, available fuel energy (kJ m^{-2}); R_{tot}, combustion rate (kW m^{-2}); d, depth of the combustion zone (m); τ, flame residence time (s); *FRP*, Fire Radiative Power (kW); *FRPD*, FRP Density (kW m^{-2}); *FRED*, Fire Radiative Energy Density (kJ m^{-2}); $I_{B,rad}$, the radiative portion of $I_{B,tot}$; $I_{B,rad}^{\text{FRED-ROS}}$, $I_{B,rad}$ produced by Eqn 7; $I_{B,rad}^{\text{FRPD-FD}}$, $I_{B,rad}$ produced by Eqn 8; t, the instantaneous time step of the image; R_{rad}, the radiative portion of R_{tot}; i, a pixel indicator along d; Δd, distance along d subtended by one pixel (m); Δ_p, pixel resolution (m); (Δx_d, Δy_d), length (pixels) of the x and y components of the flame depth vectors; $I_{B,rad}^{\text{FRP-FFL}}$, $I_{B,rad}$ produced by Eqn 9; l, length of the flame front (m); *radF*, the unitless radiative fraction

Reference	Formulation
1	$I_{B,tot} = H_{tot} w r$
2	$I_{B,tot} = E_{tot} r$
3	$I_{B,tot} = R_{tot} d$
4	$\text{ROS} = d/\tau$
5	$H_{tot}\left(\frac{\text{kJ}}{\text{kg}}\right) w\left(\frac{\text{kg}}{\text{m}^2}\right) r\left(\frac{\text{m}}{\text{s}}\right) = E_{tot}\left(\frac{\text{kJ}}{\text{m}^2}\right) r\left(\frac{\text{m}}{\text{s}}\right) = \frac{E_{tot}\left(\frac{\text{kJ}}{\text{m}^2}\right) d(\text{m})}{\tau(\text{s})} = R_{tot}\left(\frac{\text{kW}}{\text{m}^2}\right) d(\text{m})$
6	$I_{B,rad}^{\text{FRED-ROS}} = (FRED)(\text{ROS})$
7	$I_{B,rad}^{\text{FRED-ROS}} = \int_{\tau} FRPD(t)\, dt \text{ROS}$
8	$I_{B,rad} = R_{rad} d \;\rightarrow\; I_{B,rad}^{\text{FRPD-FD}} = \sum_i FRPD_i \Delta d = \sum_i FRPD_i \left(\Delta_p \sqrt{(\Delta x_d)^2 + (\Delta y_d)^2}\right)$
9	$I_{B,rad}^{\text{FRP-FFL}} = \frac{\sum FRP}{l}$
10	$I_{B,tot} = \frac{I_{B,rad}}{radF}$

Table 2. Comparison of infrared imagers used during the two separate campaigns

Data	2013	2014
Infrared imager	Agema 550	FLIR SC6703
Detector array	320 × 240	640 × 512
Spectral band	Narrow 3.9-µm filter	Narrow 3.9-µm filter

Dynamic range	473–1073 K	423–1123 K
Integration	Single	Superframing three temperature ranges
Temporal resolution	3 Hz	45 Hz (15 Hz post superframing)
Baseline spatial resolution	0.03 m	0.01 m

Table 3. Fuel type specific parameters (±1 s.d.) for longleaf pine (*Pinus palustris*), the primary fuel used in this study

Parameter	Mean (standard deviation)	Units	Number of samples
Surface area to volume ratio	59.95 (13.98)	cm^{-1}	92
Density	756.44 (454.74)	$kg\ m^{-3}$	38
Mineral content	0.001 (0.001)	g mineral per g fuel	3
Heat of combustion	20.696 (0.378)	$MJ\ kg^{-1}$	3
Low heat of Combustion	19.433–0.024 (GMC)	$MJ\ kg^{-1}$	3

Table 4. Preburn fuel bed characteristics collected for each fire in this study; gravimetric moisture content is percentage by dry weight

Standard deviations presented in parentheses

Date	Burn	Fuel load ($kg\ m^{-2}$)	Fuel depth (m)	Gravimetric moisture content (%)
7 June 2013	1	0.988 (0.028)	0.122 (0.001)	7.3 (1.2)
	2	0.972 (0.041)	0.120 (0.010)	9.4 (1.6)
9 June 2013	1	0.977 (0.018)	0.098 (0.008)	8.0 (2.5)
12 June 2013	1	0.918 (0.048)	0.102 (0.001)	7.9 (1.1)
	2	0.911 (0.078)	0.074 (0.002)	6.3 (0.6)
	3	1.296 (0.060)	0.133 (0.002)	9.6 (1.0)
14 June 2013	1	0.838 (0.040)	0.106 (0.003)	5.9 (1.1)
16 June 2013	1	0.878 (0.098)	0.114 (0.003)	11.1 (1.3)
	2	0.894 (0.056)	0.083 (0.001)	8.4 (1.4)
	3	0.878 (0.032)	0.094 (0.005)	8.7 (1.1)
18 June 2013	1	0.851 (0.022)	0.102 (0.006)	9.6 (2.2)
	2	1.282 (0.080)	0.136 (0.007)	9.0 (0.8)
	3	1.376 (0.023)	0.081 (0.007)	9.5 (1.3)
	4	0.915 (0.032)	0.080 (0.006)	10.4 (1.4)
	5	0.906 (0.059)	0.061 (0.008)	9.3 (3.3)
	6	1.347 (0.042)	0.126 (0.006)	9.7 (0.4)
	7	0.634 (0.026)	0.063 (0.003)	10.7 (0.8)
	8	1.401 (0.003)	0.153 (0.007)	8.9 (1.4)
26 Aug 2014	1	1.336 (0.012)	0.099 (0.015)	13.1 (1.1)
	3	1.120 (0.019)	0.090 (0.015)	12.0 (1.9)
27 Aug 2014	1	1.165 (0.013)	0.107 (0.013)	11.9 (1.2)
	4	1.183 (0.097)	0.085 (0.015)	13.5 (1.8)

Table 5. Mean and standard deviation of fire behaviour parameters collected for each fire conducted in this study

Fire intensity class is provided using the Canadian Forest Fire Behaviour Prediction System (CFFBPS) field guide intensity classes (IC) for describing fire behaviour based on $I_{B,tot}$ ranges (Taylor *et al*. 1997). Standard deviations presented in parentheses

Date	Burn	Low heat of combustion (kJ kg^{-1})	Fuel consumption (kg m^{-2})	Rate of spread (m s^{-1})	Fire intensity (kW m^{-1})	IC
7 June 2013	2	19 206 (38)	0.842 (0.045)	0.013 (0.022)	207.9 (361.9)	2
9 June 2013	1	19 240 (60)	0.885 (0.033)	0.013 (0.046)	235.0 (781.8)	2
12 June 2013	1	19 242 (28)	0.822 (0.042)	0.156 (0.099)	2353.6 (1566.0)	4
	2	19 280 (15)	0.758 (0.052)	0.039 (0.056)	549.4 (829.7)	3
	3	19 200 (25)	1.134 (0.047)	0.025 (0.031)	539.7 (690.2)	3
14 June 2013	1	19 290 (26)	0.767 (0.049)	0.013 (0.034)	205.9 (487.9)	2
16 June 2013	1	19 166 (33)	0.732 (0.108)	0.026 (0.046)	418.6 (692.3)	2
	2	19 231 (34)	0.803 (0.063)	0.052 (0.057)	847.4 (899.4)	3
	3	19 223 (26)	0.762 (0.006)	0.047 (0.042)	691.3 (614.7)	3
18 June 2013	1	19 201 (54)	0.799 (0.030)	0.014 (0.031)	235.6 (472.5)	2
	2	19 216 (19)	1.155 (0.102)	0.065 (0.081)	1301.6 (1792.1)	3
	3	19 204 (33)	1.248 (0.022)	0.013 (0.026)	314.7 (629.8)	2
	4	19 181 (35)	0.817 (0.027)	0.013 (0.044)	211.1 (681.3)	2
	5	19 209 (79)	0.770 (0.056)	0.013 (0.025)	207.5 (376.9)	2
	6	19 199 (10)	1.220 (0.038)	0.017 (0.033)	415.8 (784.1)	2
	7	19 174 (19)	0.582 (0.033)	0.065 (0.063)	747.3 (715.7)	3
	8	19 217 (34)	1.270 (0.027)	0.026 (0.037)	636.9 (909.0)	3
26 Aug 2014	1	19 217 (26)	1.225 (0.042)	0.073 (0.068)	1719.0 (1576.4)	3
	3	19 243 (46)	0.950 (0.060)	0.047 (0.058)	859.6 (1047.2)	3
27,Aug 2014	1	19 245 (33)	1.058 (0.092)	0.032 (0.055)	666.5 (1120.1)	3
	4	19 207 (45)	1.104 (0.125)	0.029 (0.059)	622.6 (1289.1)	3

Table 6. Summary of infrared fire intensity method implementations

FI_{rad} resolution describes the actual data available from each method, Output format refers to degraded data used only for comparison with ground sampling. FRP-FFL, Fire Radiative Power–Flame Front Length; FRPD-FD, Fire Radiative Power Density–Flame Depth; ROS, rate of spread; FRPD, FRP density; FRED, fire radiative energy density

Method	Imagery requirements	Radiant energy	Sampling	Measurement	FI_{rad} resolution	Output format
FRP-FFL	Individual frames	FRP (kW pixel^{-1})	Summed for entire image (and also for flaming area separately)	Flame front identified by fixed threshold (773 K). Length measured from north to south on platform	Single value for each frame	Median by row
FRED-ROS	Time series	FRPD (kW m^{-2})	Integrated over time series for each pixel	ROS computed for perimeter pixels using Paugam *et al.* (2013) and 773 K arrival threshold	Value for each pixel where ROS was computed	Median by row
FRP-FD	Individual frames	FRPD (kW m^{-2})	Integrated along the normal extending from the perimeter into the flame depth	Flame front identified by fixed threshold (773 K). At 0.5-m spacing, flame depth is measure initiated following the normal and	Values at 0.5-m spacing along flame front	Median by row

terminated where two consecutive pixels fall below the termination threshold (773 and 700 K used)

Table 7. Testing the deviation from the line of perfect agreement of regressions in Figs 9, 10 and 11

The column '95% CI' indicates if the line of perfect agreement (LPA) is within (w), below (b) or above (a) the 95% confidence interval (CI); multiple values indicate partial containment within the 95% CI. FRED, fire radiative energy density; FD, Flame Depth; ROS, rate of spread

Method	Figure	Radiative fraction	R^2	slope	s.e.	Critical *t*	d.f. (n – 2)	*t*	*P*	95% CI
FRPD-FD	9*a*	0.26	0.45	0.70	0.27	2.31	8	1.11	0.299	w
FRPD-FD	9*b*	0.24	0.45	0.76	0.30	2.31	8	0.80	0.447	w
FRPD-FD	9*c*	0.17	0.45	1.06	0.42	2.31	8	–0.14	0.892	w
FRED-ROS	10*a*	0.21	0.91	0.68	0.04	2.06	25	8.00	<0.0001	w, a
FRED-ROS	10*b*	0.17	0.91	0.84	0.05	2.06	25	3.20	0.0037	w, a
FRED-ROS	10*c*	0.15	0.91	0.96	0.06	2.06	25	0.67	0.5090	w
FRED-ROS	11*a*	0.21	0.34	0.69	0.20	2.06	25	1.55	0.134	w
FRED-ROS	11*b*	0.17	0.34	0.85	0.24	2.06	25	0.63	0.535	w
FRED-ROS	11*c*	0.15	0.34	0.97	0.28	2.06	25	0.11	0.913	w

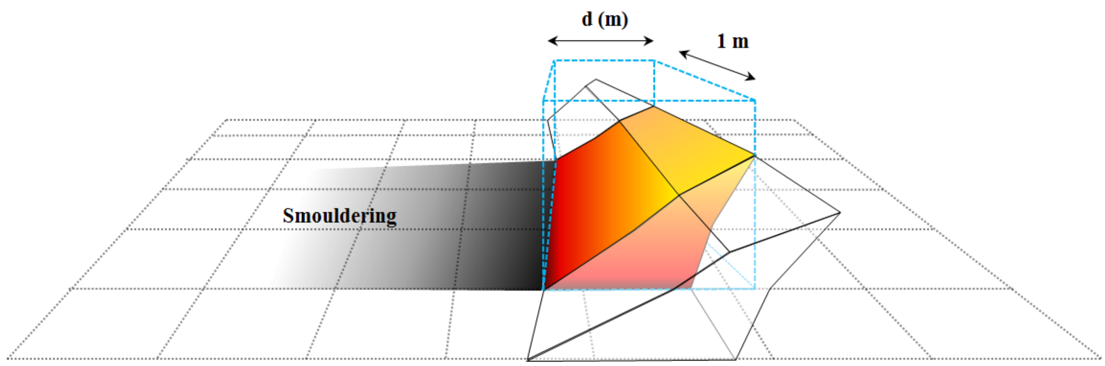

Fig. 1. Visualisation of Byram's fire intensity ($I_{B,tot}$; kW m^{-1}) in a spreading fire. For any unit length of the flame front (m) $I_{B,tot}$ represents the energy release (kW) of the fire extending inward from the leading edge for the full depth of the active reaction zone (*d*; flame depth). The energy released owing to smouldering after the fire front passage does not contribute to the intensity of the flame front, and so it is not included in the calculation of $I_{B,tot}$.

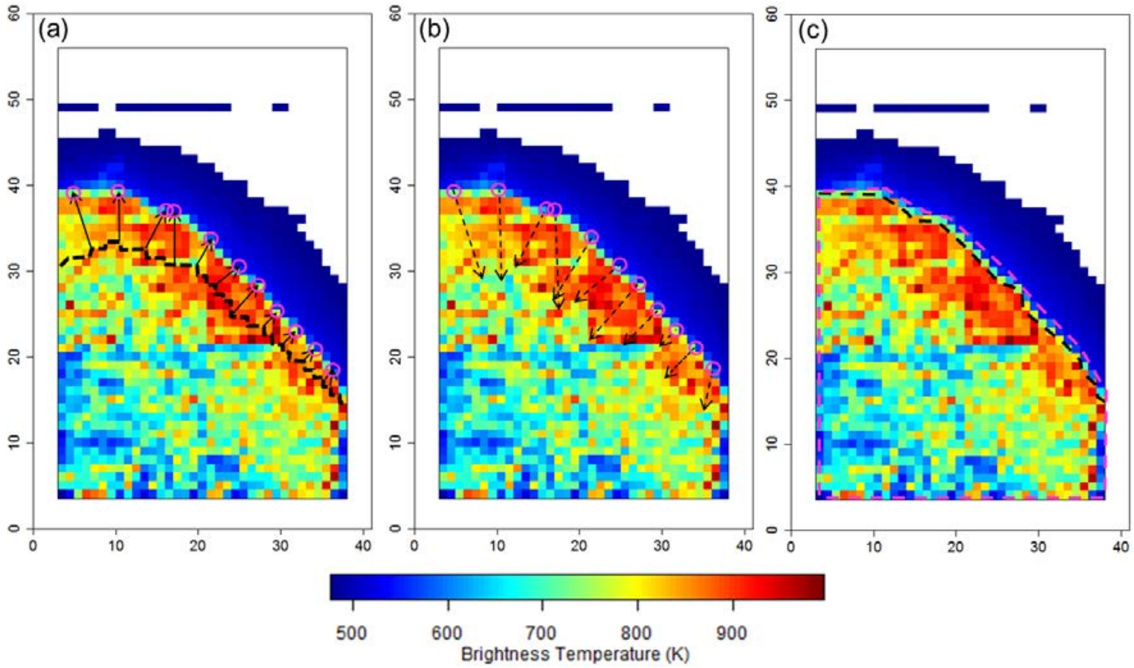

Fig. 2. Visualisation of the measurement and sampling approaches used within the different methods ((*a*) Fire Radiative Energy Density - Rate of Spread (FRED-ROS), (*b*) Fire Radiative Power Density-Flame Depth (FRPD-FD) and (*c*) Fire Radiative Power-Flame Front Length (FRP-FFL)) for calculating radiative fire intensity from thermal infrared imagery applied herein. Note: sample points and vectors are illustrative and do not represent all the pixels that would be sampled on the exemplar image. In (*a*), the FRED-ROS method integrates the measured FRPD (kW m^{-2}) over the time series at each fire perimeter pixel location (pink circles) to produce FRED (kJ m^{-2}), and combines this with rate of spread measured along the normal (black arrow) from the perimeter at the previous time step (dotted black line) at each sample point. In (*b*), the FRPD-FD method sums all FRPD (kW m^{-2}) along the normal (dotted black arrows) extending inward into the flame body from individual perimeter pixels (pink circles), the length of these vectors is measured to determine the flame depth (FD) at each perimeter location and the FRPD and FD are combined as in Eqn 8. In (*c*), the FRP-FFL method sums all FRP (kW) for the entire fire (outlined in pink dotted line) and divides this by the measured length of the flame front (black dotted line), producing a single value of radiative $I_{B,tot}$ for the entire flame front. Notably, a horizontal line of pixels is illuminated in front of the flame front in this example image; this is caused by IR radiation from the fire heating an overhead cable connected to other instrumentation not used in this study, artefacts such as these were masked out of analysis.

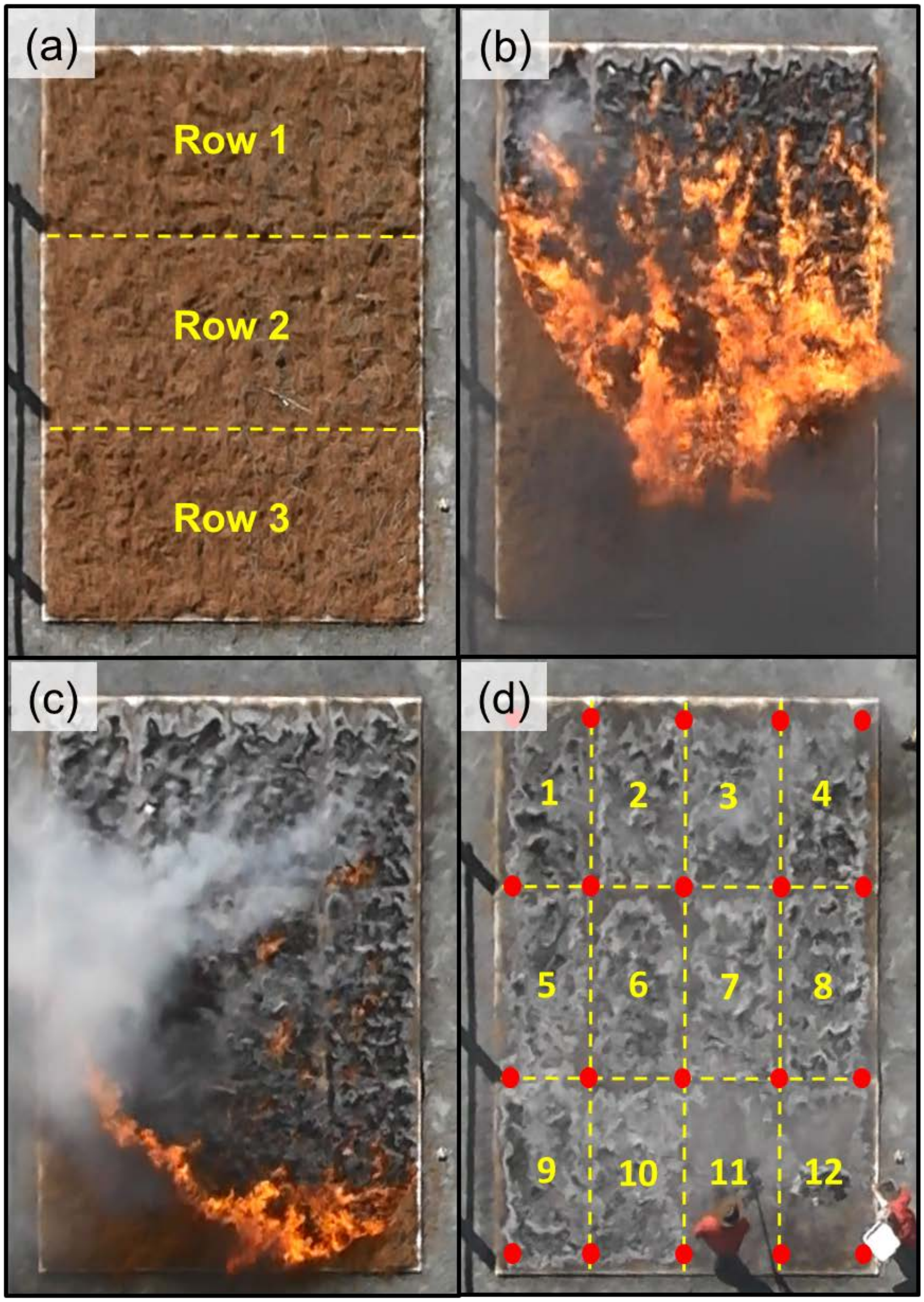

Fig. 3. Exemplar visible imagery of the 26 August 2014 Burn 1 experiment (Table 5), collected from camera viewing from the 30-m high tower shown in Fig. 4 and taken (*a*) 10; (*b*) 50; (*c*) 120; and (*d*) 300 s after initial ignition respectively. In (*a*), the position of the rows is identified, and the numbering of panels is found in (*d*). Red dots in (*d*) indicate the location of fuel bed thermocouples used for rate of spread sampling for independent comparison.

Publisher: CSIRO; Journal: WF:International Journal of Wildland Fire
Article Type: research-article; Volume: ; Issue: ; Article ID: WF16178
DOI: 10.1071/WF16178; TOC Head:

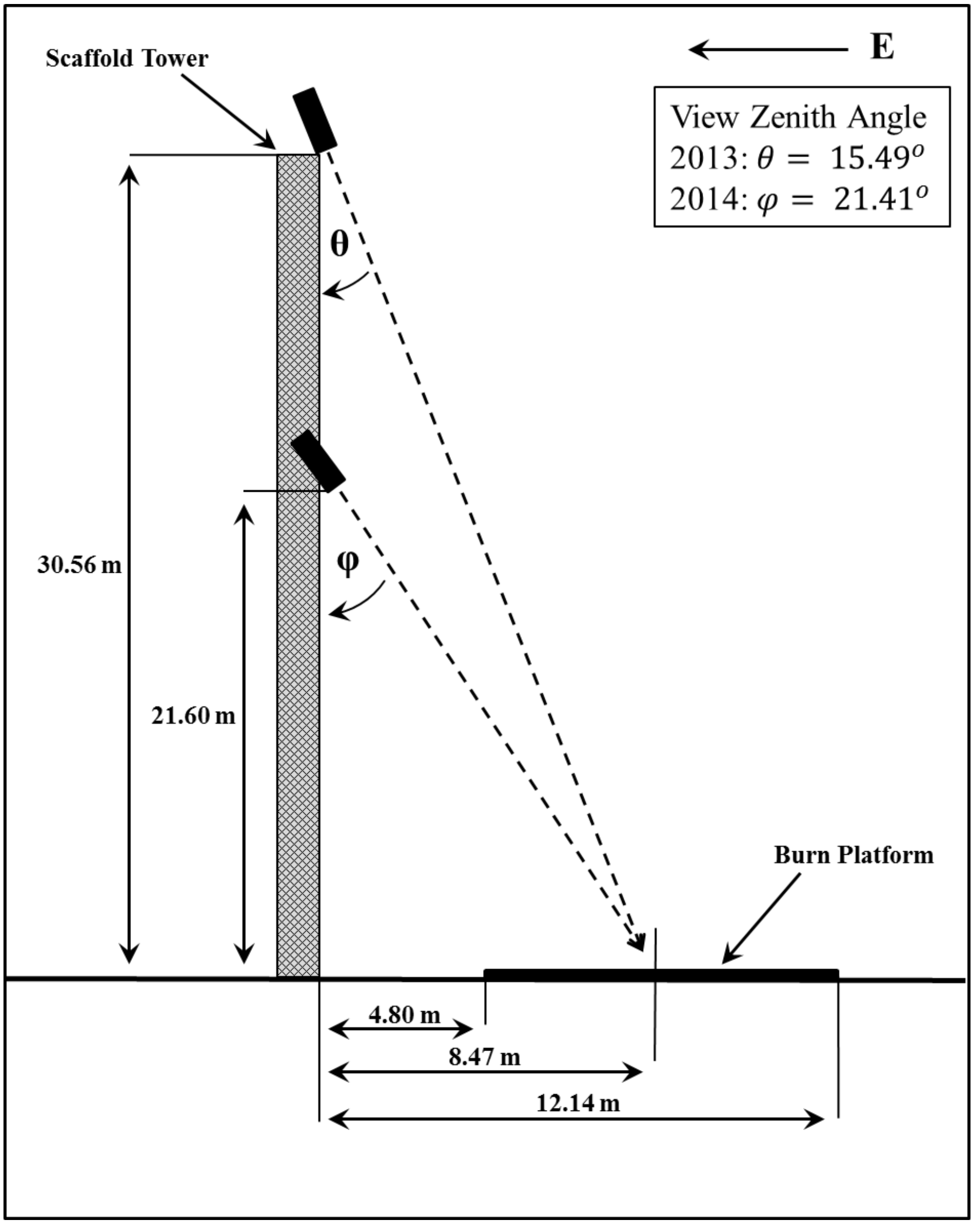

Fig. 4. Positioning of scaffold tower relative to the burn platform (not to scale). Placement of the mid-wave infrared (MWIR) camera in 2013 and 2014 gave a view zenith angle to the centre of the burn platform of 15.49° and 21.41° respectively. At this range, raw spatial resolutions (averaged over the platform) were 0.035 and 0.015 m for 2013 and 2014 respectively.

Publisher: CSIRO; Journal: WF:International Journal of Wildland Fire
Article Type: research-article; Volume: ; Issue: ; Article ID: WF16178
DOI: 10.1071/WF16178; TOC Head:

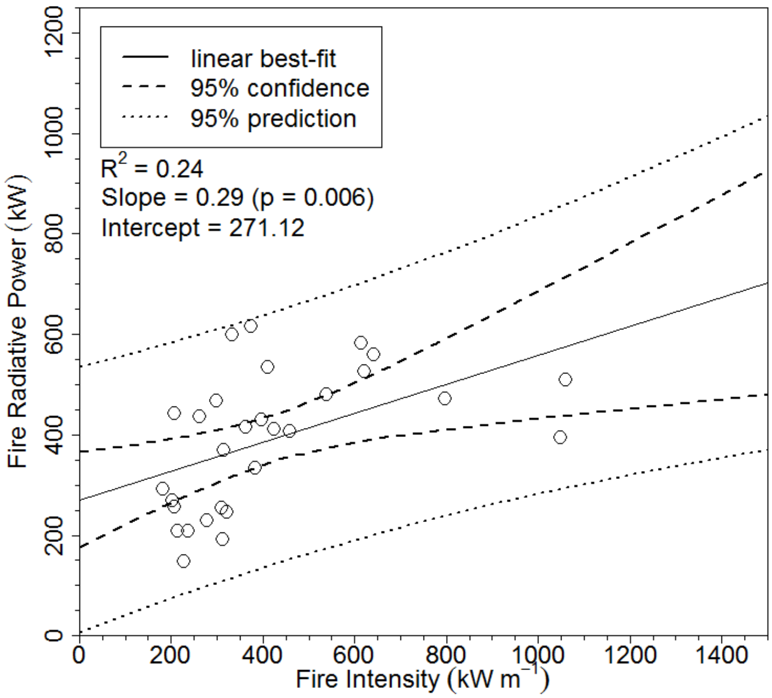

Fig. 5. Total Fire Radiative Power (FRP; kW) averaged by row (Fig. 3*a*) and compared with $I_{B,tot}$ (kW m^{-1}) calculated using IR rate of spread (ROS) and Eqn 1 by row for the 2013 experimental burns (for fires which contained the full depth of the reaction zone within the burn platform). Values from Row 1 were removed owing to incomplete flame front presence (and therefore reduced FRP) and contamination by drip torch fuel from the ignition line.

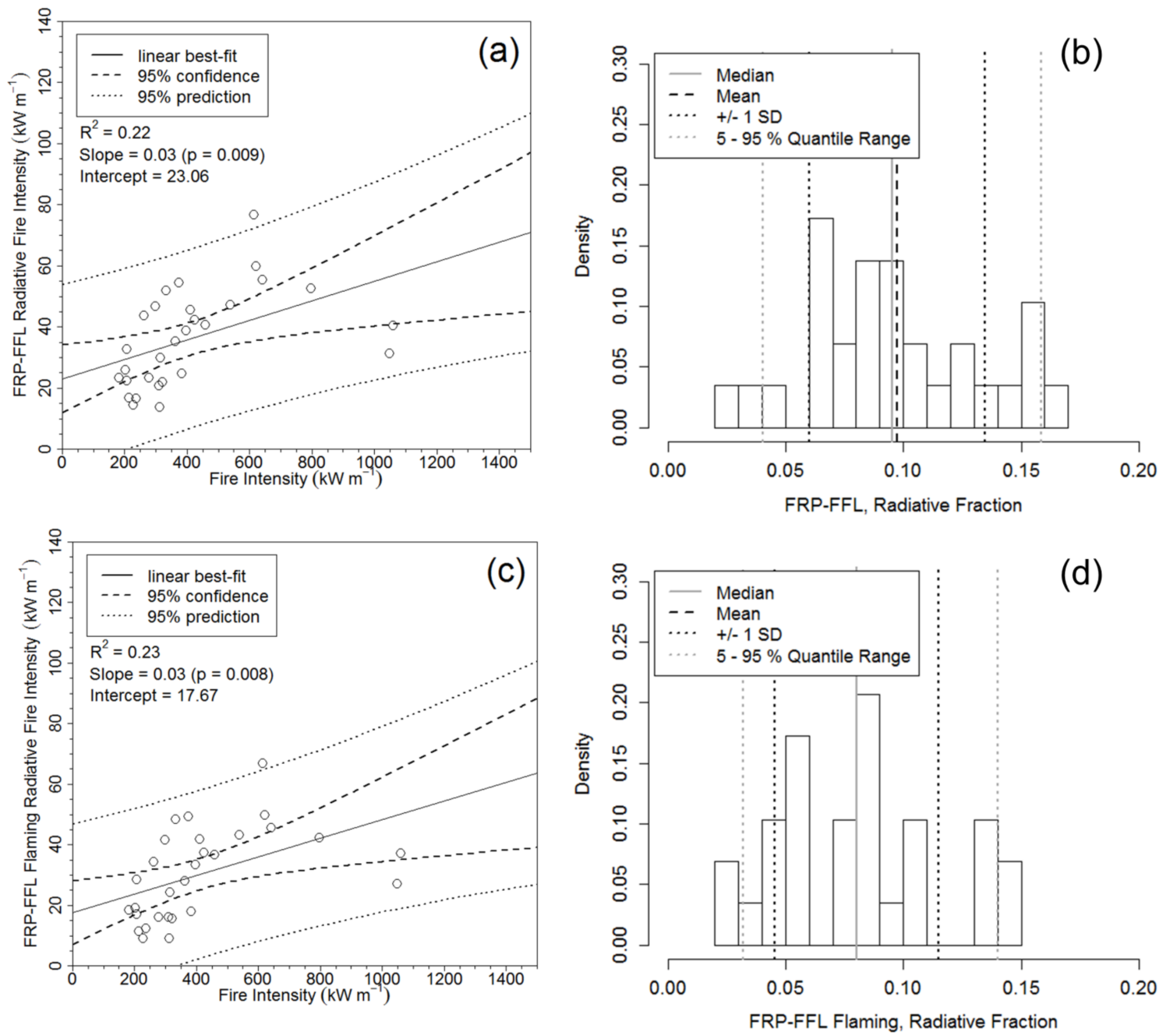

Fig. 6. Linear regression between $I_{B,tot}$ and $I_{B,rad}$ generated using the Fire Radiative Power-Flame Front Length (FRP-FFL)method (*a*), and the same method while only sampling FRP in the flaming zone (*c*). Frequency distribution of the radiative fractions computed by dividing $I_{B,rad}$ produced by the FRP-FFL method (*b*), and the same method limited to the flaming zone (*d*) by $I_{B,tot}$ for all data points presented in (*a*) and (*c*) respectively. The data used here were gathered using the 2013 burns and were sampled by row of the burning plot (Fig. 3a). Row 1 was removed from analysis owing to contamination with the ignition fuels and to its inability to fully represent the flame depth owing to the acceleration stage of the fire. In (*b*), the mean value is 0.10 with a standard deviation of 0.04, the median is 0.10, and the 5 and 95% quantile ranges are 0.04 and 0.16 respectively. In (*d*), the mean value is 0.08 with a standard deviation of 0.03, the median is 0.08, and the 5 and 95% quantile ranges are 0.03 and 0.14 respectively.

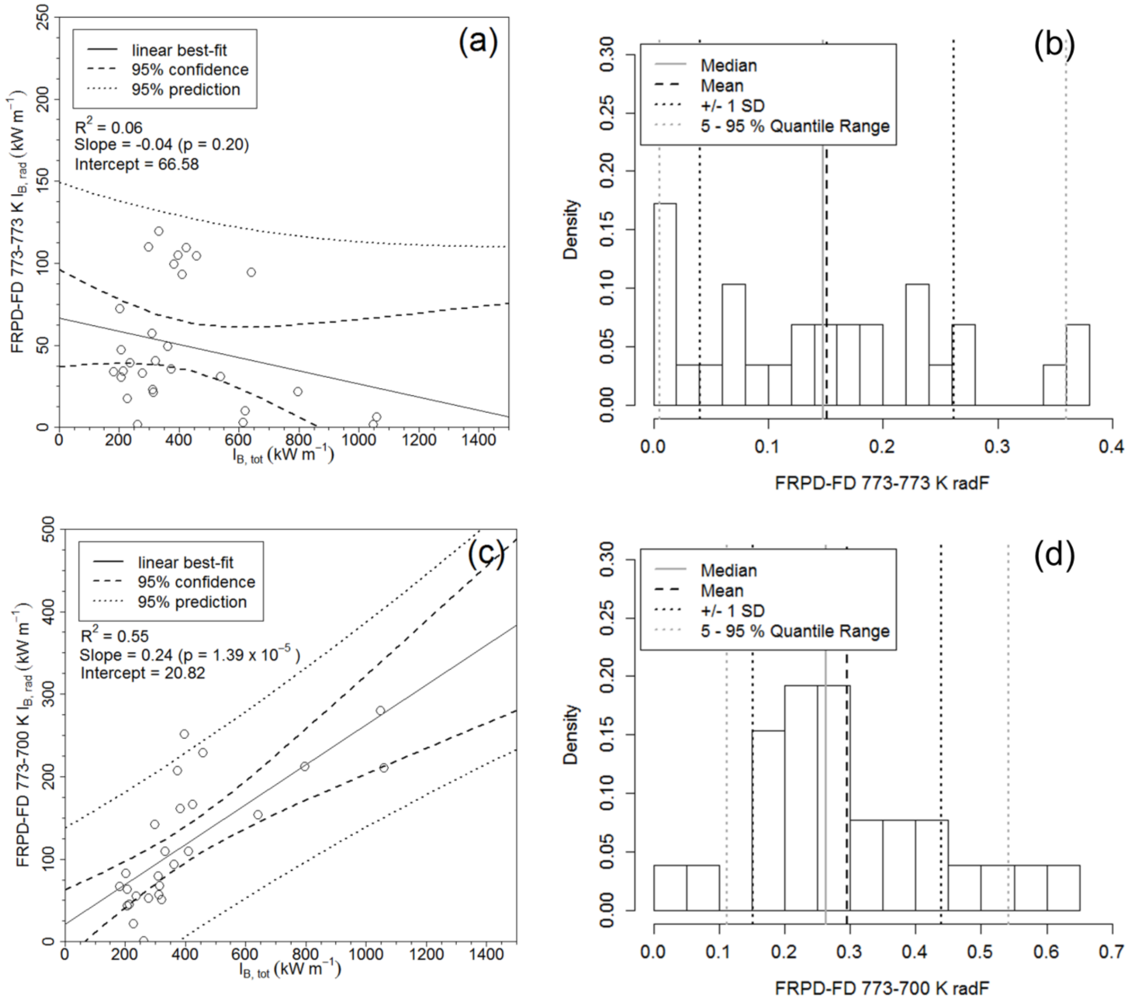

Fig. 7. Linear regression between $I_{B,tot}$ and $I_{B,rad}$ generated using the Fire Radiative Power Density-Flame Depth (FRPD-FD) method with a flame depth termination threshold of 773 K (*a*), and 700 K (*c*). Frequency distributions of the radiative fractions computed by dividing $I_{B,rad}$ produced by the FRPD-FD method with a flame depth termination threshold of 773 K (*b*), and 700 K (d) by $I_{B,tot}$ for all data points presented in (*a*) and (*b*) respectively. The data used here were gathered during the 2013 burns and sampled using medians by row of the burning plot (Fig. 3*a*). Row 1 was removed from analysis owing to contamination with the ignition fuels and the absence of full flame depth. In (*b*), the mean value is 0.15 with a standard deviation of 0.11, the median is 0.14, and the 5 and 95% quantile ranges are 0.005 and 0.36 respectively. In (*d*), the mean value is 0.29 with a standard deviation of 0.14, the median is 0.26, and the 5 and 95% quantile ranges are 0.11 and 0.54 respectively.

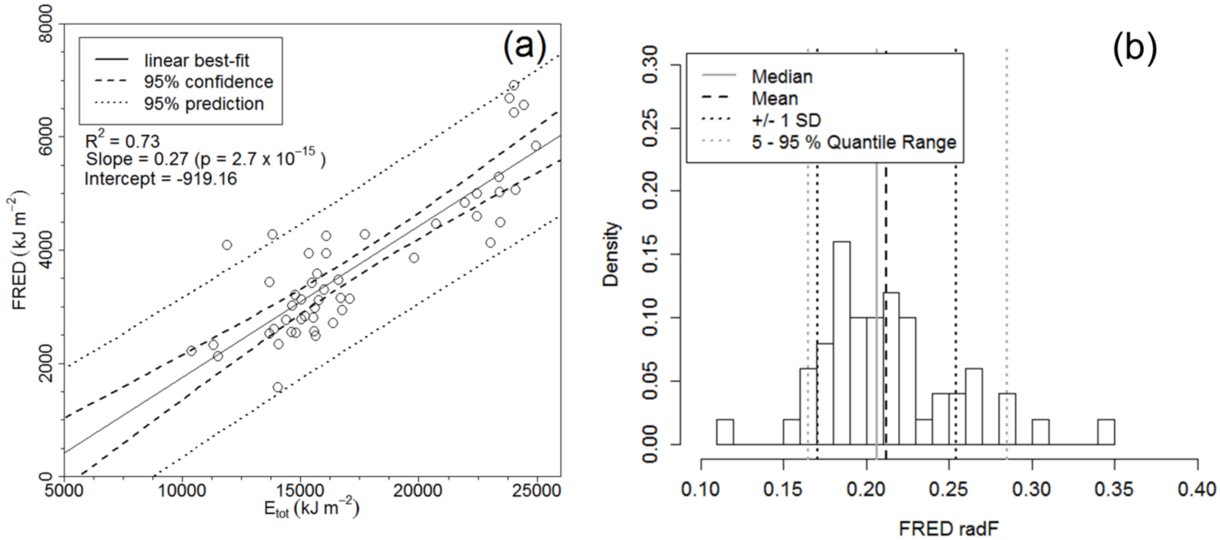

Fig. 8. Linear regression between the ground-sampled available fuel energy (E_{tot} ;kJ m^{-2}) and the Fire Radiative Energy Density (FRED; kJ m^{-2}) measured in the Fire Radiative Energy Density - Rate of Spread (FRED-ROS) method (*a*). Frequency distribution of the radiative fractions computed by dividing FRED (kJ m^{-2}) produced by the FRED-ROS method by the E_{tot} of $I_{B,tot}$ (*b*) for all data points presented in (*a*). The data used here were gathered using the 2013 burns and are presented as mean value of pixel FRED and ground-sampled low heat of combustion scaled by fuel consumption for each row to produce E_{tot}. Row 1 was removed from analysis owing to contamination with the ignition fuels. In (*b*), the mean value observed here is 0.21 with standard deviation of 0.04, the median is 0.20, and the 5 and 95% quantile ranges are 0.16 and 0.28 respectively.

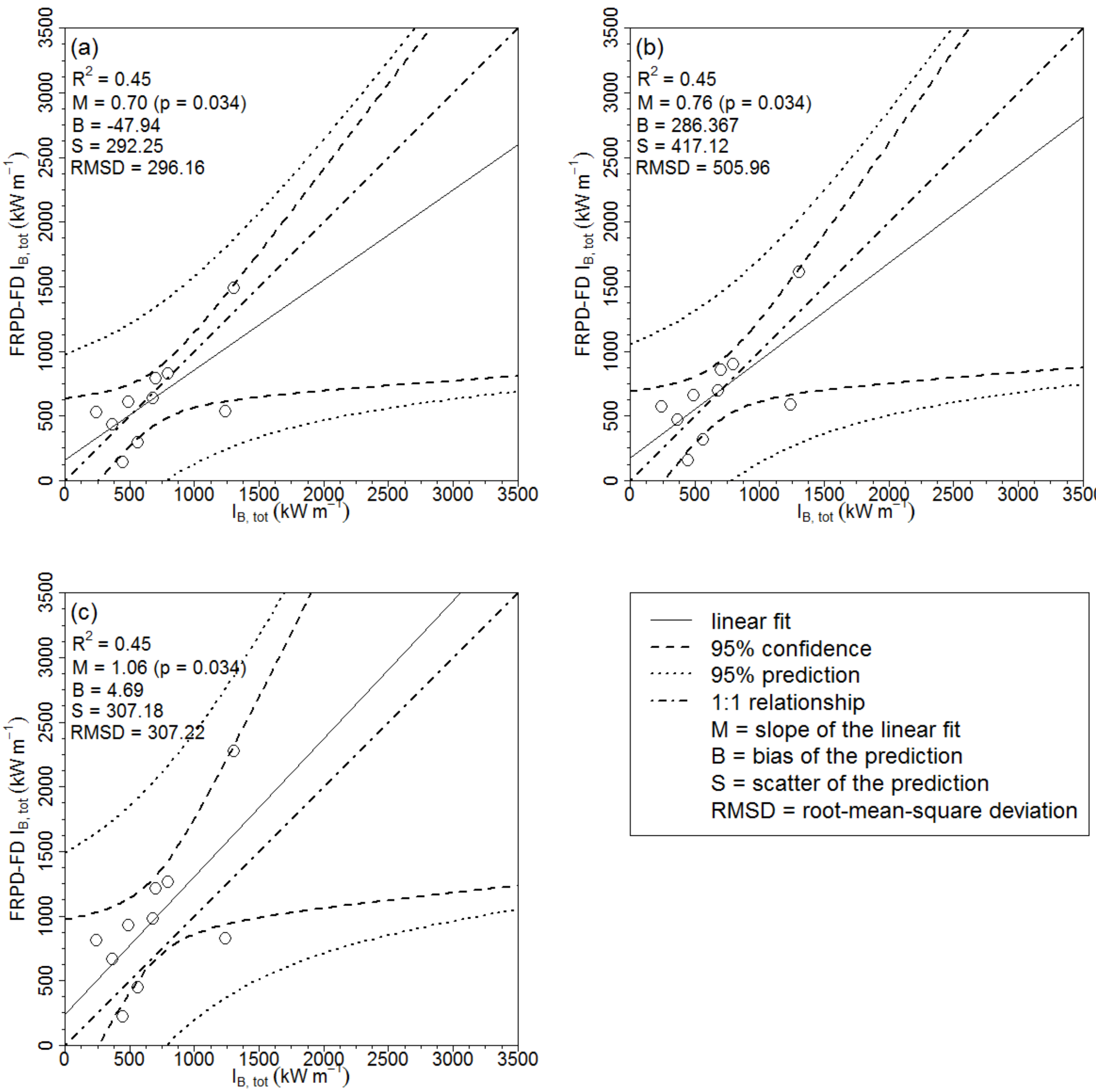

Fig. 9. Linear regression between $I_{B,tot}$ and $I_{B,tot}$ generated using the FRPD-FD method with three different radiative fraction corrections; (*a*) 0.26; (*b*) 0.24; and (*c*) 0.17. The intent of this comparison is to identify which radiative fraction best approximates the line of perfect agreement (LPA; Table 7). The data used here were gathered from the 2014 burns and were sampled using median values for each by panel. Row 1 was removed from analysis owing to contamination with the ignition fuels, panels were removed from analysis if it was not possible to calculate $I_{B,tot}$ using this method (e.g. inability to measure flame depth owing to it reaching a platform boundary).

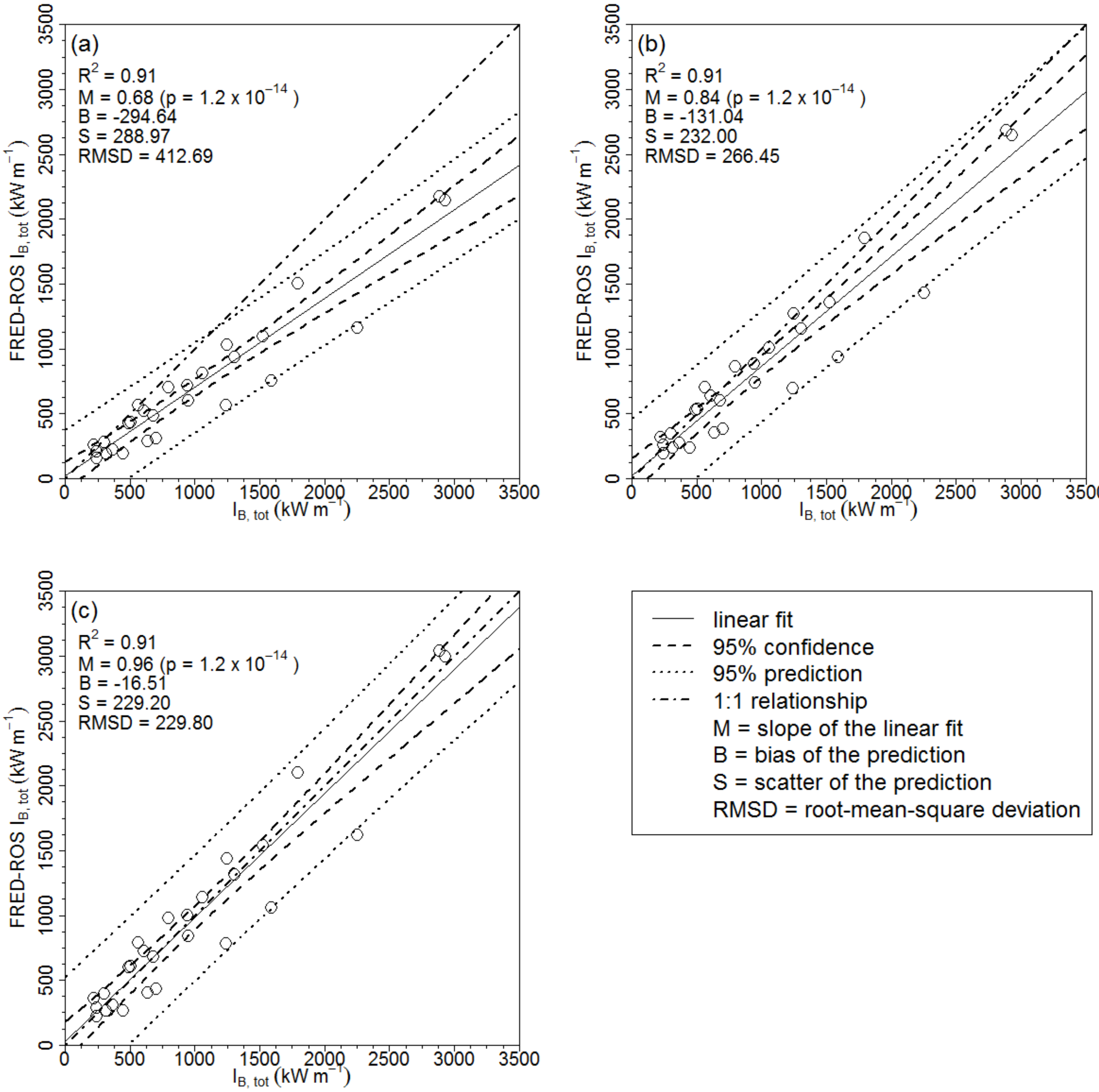

Fig. 10. Linear regression between $I_{B,tot}$ and $I_{B,tot}$ generated using the FRED-ROS method with three different radiative fraction corrections; (*a*) 0.21; (*b*) 0.17; and (*c*) 0.15. ROS used for $I_{B,tot}$ and the FRED-ROS $I_{B,tot}$ are not independent, resulting in the strong agreement found here. The intent of this comparison is not to assess this agreement, but rather to identify which radiative fraction best approximates the line of perfect agreement (LPA; Table 7). The data used here were gathered using the 2014 burns and sampled using median values for each by row. Row 1 was removed from analysis owing to contamination with the ignition fuels.

Publisher: CSIRO; Journal: WF:International Journal of Wildland Fire
Article Type: research-article; Volume: ; Issue: ; Article ID: WF16178
DOI: 10.1071/WF16178; TOC Head:

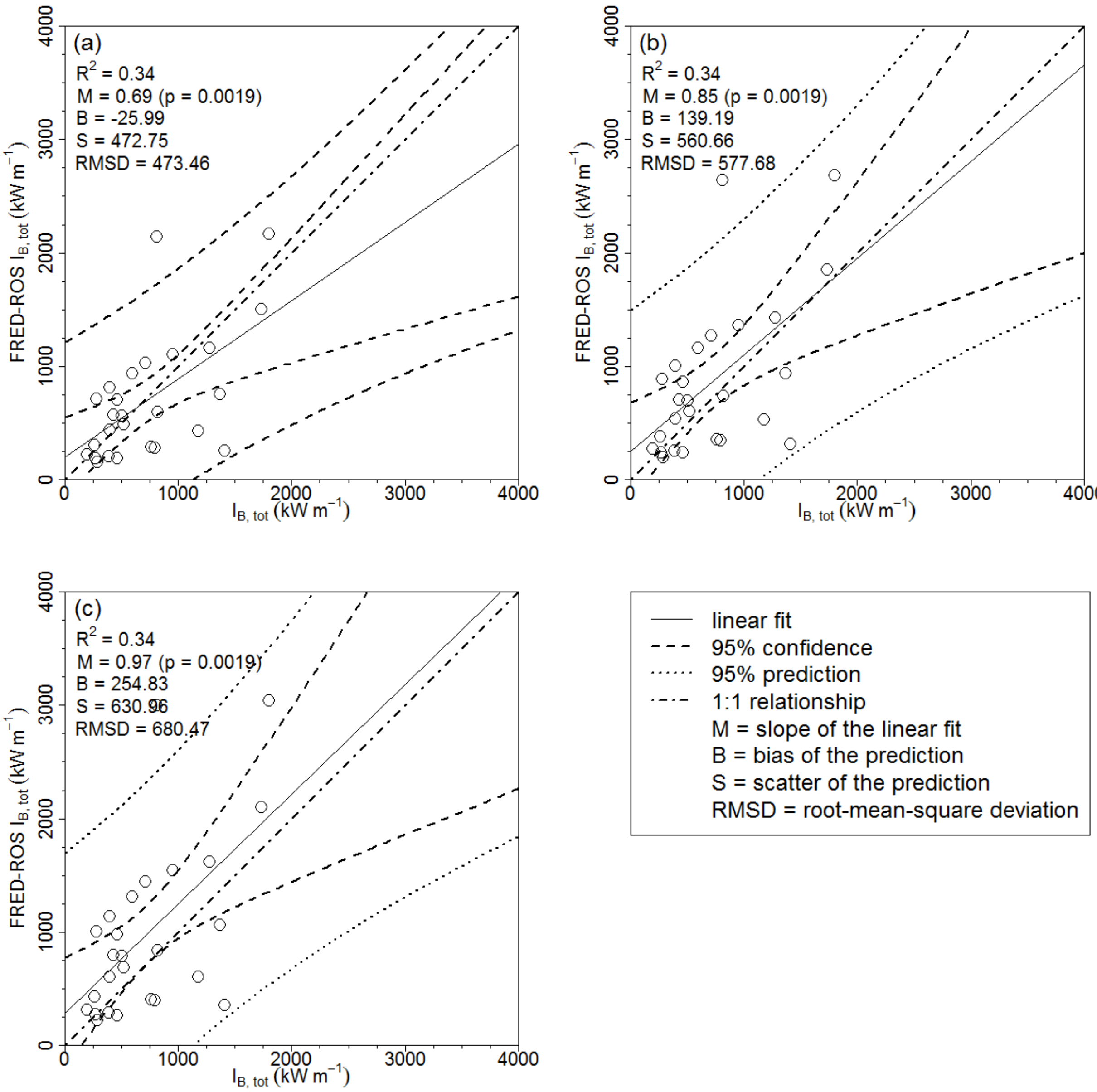

Fig. 11. Linear regression between $I_{B,tot}$ calculated with an independent ROS measurement method (thermocouple grid ROS) and $I_{B,tot}$ generated using the FRED-ROS method with three different radiative fraction corrections; (*a*) 0.21; (*b*) 0.17; and (*c*) 0.15. The intent of this comparison is to identify which radiative fraction best approximates the line of perfect agreement (LPA; Table 7). The data used here were gathered using the 2014 burns and sampled using median values for each panel. Row 1 was removed from analysis owing to contamination with the ignition fuels.

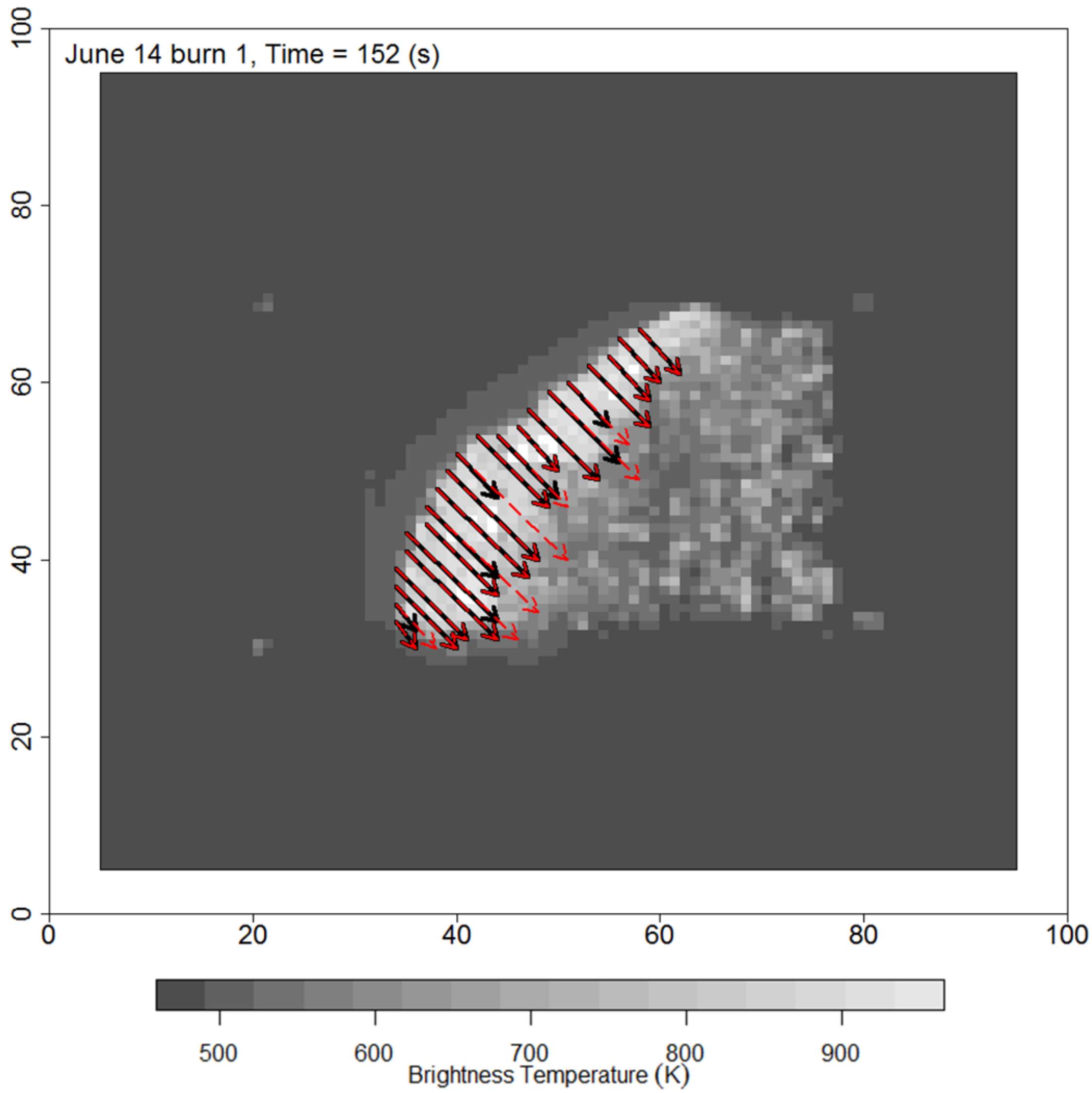

Fig. 12. Flame depth vectors estimated using the FRPD-FD method and a flame depth termination threshold temperature of 773 K (black arrows) and 700 K (red dotted arrows) on the 14 June 2013 Burn 1 of the 2013 experimental campaign (Table 5), 152 s after fire ignition. Data collected with the Agema 550 thermal imager from a distance of 30.9 m, with the brightness temperatures shown calculated using a unitary atmospheric transmissivity and emissivity. As can be seen where the temperature threshold is higher (black arrows), on occasion, this measurement stops early when there is some flame depth remaining to be measured, whereas the lower threshold (red dotted arrows) allows the flaming zone (area of increased brightness temperature adjacent to the leading edge of the fire) to be sampled and occasionally allows the measurement to continue into the non-flaming zone (area of cooler brightness temperatures that trails behind the flame front and remains above ambient background temperature).

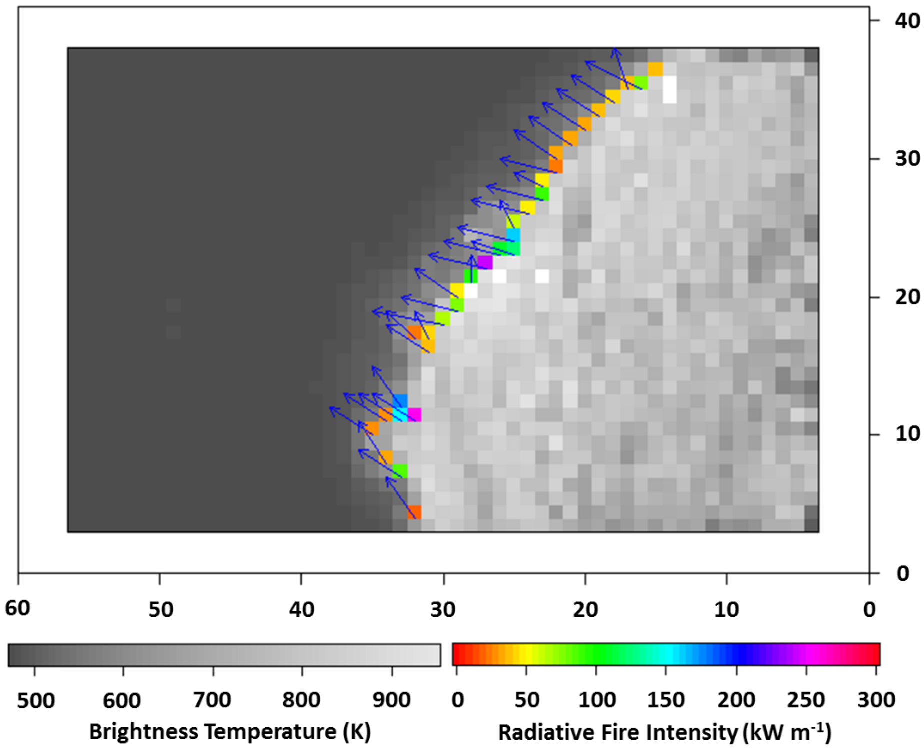

Fig. 13. Depiction of outputs from the Fire Radiative Energy Density - Rate of Spread (FRED-ROS)calculation of $I_{B,rad}$. The georeferenced infrared imagery is used to calculate FRPD (kW m^{-2}) at each time step and is integrated at each pixel to produce FRED (kJ m^{-2}). The infrared time series is also employed for calculation of ROS and direction of spread (blue arrows) at each time step. The FRED and ROS values are then combined at each point along the flame front to produce the FI_{rad} spatially wherever the ROS method produces measurements (coloured pixels).

[A]Linear regression of the Fire Radiative Power-Flame Front Length (FRP-FFL) and Fire Radiative Power Density-Flame Depth (FRPD-FD) methods were not significant (adj. R^2 = 0.39 and 0.17, P = 0.08 and 0.69 respectively), so the stepwise approach was not used for those two methods.